ABSTRACT

SHIVA, TEJA KONETI. Jet Impingement Heat Transfer on Additively Manufactured Cylindrical Micro Roughness Elements – Effect of Surface Imperfections. (Under the direction of Dr. Srinath V. Ekkad).

The demand for faster and more efficient computing is increasing rapidly and cooling these electronics is of utmost importance. Components of electronics like transistors, microprocessors, System on Chips (SoC) generate heat over time and have to be cooled for better performance and an extended lifespan. Current state-of-the-art systems use jet impingement and/or extended surfaces to enhance the cooling of high density electronics. With the advent of new additive manufacturing(AM) techniques like Direct Metal Laser Sintering (DMLS), extended surfaces as small as ~500 μm thick can be manufactured. Present work mainly focuses on the performance of cylindrical micro pin fins printed on a smooth surface using DMLS technique. AM techniques involve merging solid particles together and this process alters the microstructures of the material leading to undesired surface features. Therefore, numerical studies involving the intended design may lead to erroneous results. In this study, the need for improving numerical techniques and 3D Computer Aided Design (CAD) models to better predict the real world performance is addressed. Experimental and numerical analysis were performed for the cylindrical micro pin fins of the order of 500 microns. Jet to target plate spacing $Z/D_{jet} = 1$ and jet to jet spacing of $X/D_{jet} = 3$ were used with an array of 5×5 jets impinging on to a plate of dimension $50.8\, mm \times 50.8\, mm \times 3.175\, mm$. The flow Reynolds number based on individual jet diameter was varied from 3000 to 12000. However, numerical analysis of intended geometry overpredicted Nusselt number by an average of about 32% over the experimental value. The discrepancy in the results was due to the undesired surface features (interconnections between the micro pin fins) incurred while manufacturing the sample by DMLS method. These interconnections were then characterized using optical scans from a confocal laser microscope. A new geometry was reconstructed from the data obtained from the profilometry. Numerical analysis with the modified geometry that included the surface imperfections were able to better predict the heat transfer trends. The global Nusselt number predicted here is 25% more accurate than the simulations with the intended geometry. In addition to the cylindrical pin fins, pyramidal pin fins with a truncated top were also considered to show the deviation in the numerical analysis of intended and actual geometries. The deviation in global Nusselt number was calculated to be about 15%. A study comparing non-conjugate simulation with conjugate heat transfer simulations is also presented.

Jet Impingement Heat Transfer on Additively Manufactured Cylindrical Micro Roughness Elements – Effect of Surface Imperfections

by
Shiva Teja Koneti

A thesis submitted to the Graduate Faculty of
North Carolina State University
in partial fulfillment of the
requirements for the degree of
Master of Science

Mechanical Engineering

Raleigh, North Carolina
2021

APPROVED BY:

Dr. Alexi Saveliev

Dr. Richard Gould

Dr. Srinath V. Ekkad
Committee Chair

DEDICATION

In the loving memory of Vemanarayana,

To my family and friends

BIOGRAPHY

Shiva Teja Koneti was born and raised in India. He graduated with a Bachelor’s degree in Mechanical Engineering from Indian Institute of Technology (IIT) Delhi in the year of 2019. To further his education, he moved to United States of America to pursue Graduate studies at North Carolina State University from the Fall of 2019.

ACKNOWLEDGEMENTS

I would like to thank Dr. Srinath Ekkad for giving me the opportunity to work under him and for his unwavering support. His valuable guidance and expert advice have contributed immensely towards my holistic growth. He has always been and will continue to be a source of inspiration to me. I would also like to thank Dr. Alexi Saveliev and Dr. Richard Gould for being members in my committee.

Special thanks to Srivatsan Madhavan for all his thoughtful discussions, valuable insights, and continuous encouragement throughout my time at the Thermal Energy Research and Management Lab (ThERMaL). This work would not have been possible without his support and inputs. Many thanks to Pratik Bhansali for being my mentor throughout my master's journey. He has been available at all times to clear my doubts and has always been a constant source of motivation. I would also like to thank my lab mates Kishore, Shoaib, Ben, Sanskar, Obinna and all other members of ThERMaL for their continuous support and for making this journey memorable and joyful. I also wholeheartedly thank all my friends at NC State and in India.

My heartfelt thanks to my parents Nagaraju and Sailaja and my sister Renuka for being pillars of strength, who have always backed my decisions with utmost encouragement. I would also like to thank my grandparents for their blessings.

TABLE OF CONTENTS

LIST OF TABLES

LIST OF FIGURES

CHAPTER 1

INTRODUCTION AND BACKGROUND

The invention of semiconductors led to a revolution in technology with the advent of diodes, resistors, transistors, microprocessors, Integrated Circuits (IC) and ultimately System on Chips (SoC). These components of electronics are rapidly diminishing in size all while their intricacy and competence continue to grow at an incredible rate. This has created a dramatic surge in the power density, ensuing in rapidly escalating temperatures and a large rise in the number of circuit malfunctions. As a result, cooling of electronics has gained a lot of importance in past few decades. A phenomenon known as Joule heating is the main cause of heat generation in electronics. Electronic components are poor at conducting heat and require external intervention to cool them. The typical techniques used for cooling electronic components have been discussed in the section below.

1.1 Methods of Electronics Cooling

Thermal resistance plays a crucial role in the field of thermal management and consequently in electronics cooling. Similar to how the electrical resistance resists flow of current through a circuit, the thermal resistance opposes flow of heat. The unit of thermal resistance is $°C/W$. To put it into perspective, an electronic component rated at $10°C/W$ gets $10°C$ hotter than surroundings when it dissipates 1 W of heat. There are several methods in use to remove heat produced from electronic components. The predominantly used ones are - heat sinks, fans, thermoelectric coolers, heat pipes, and jet impingement cooling. There are three modes of heat transfer – conduction, convection, and radiation. A good thermal design for cooling electronics uses all these three components in harmony to achieve efficient cooling though one mode is always dominant. Staring with heat sinks, in reality there is only one true heat sink – the surrounding.

Blocks of aluminum on surfaces of chips in Printed Circuit Boards (PCB) are usually referred as heat sinks but are not the actual heat sinks. Thermal engineers refer to such solids as "extended surfaces", but it is not a catchy word, and the word heat sink is. Hence the discrepancy in terminology.

Figure 1.1: Heat sink on a PCB (adopted from tom's hardware - what is a heat sink? website)

Most electronics components have flat surfaces; adding extended surface on to these components provides additional surface area for the generated heat to dissipate. In doing so, they conduct heat away from the component by natural or forced convection. Other advantage of using extended surfaces is that the thermal conductivity of material used (often aluminum) is much higher than that of semiconductors, thus making it easier for heat dissipation.

Heat sinks with extended surfaces are broadly classified into passive and active heat sinks. Active heat sinks have dedicated fans attached to it, whereas passive heat sinks solely depend on surrounding air. Forced convection in active heat sinks makes them more effective at dissipating heat than passive heat sinks with make use of natural convection. Thus, fans are an integral part of cooling electronics with high power density. Fans create a pressure difference across extended surfaces and surroundings, enabling airflow through the heat sink to aid in heat removal.

Figure 1.2: Fan attached to a heat sink (picture adopted from gabrian.com)

Thermoelectric coolers that work on the reverse Seebeck or Peltier effect are also used in electronic cooling, however not as often as active/passive heat sinks. Electric current flowing through the junction of two dissimilar metals will emit or absorb heat per unit time at junction to balance the difference in chemical potential of two materials. The junction where heat is absorbed is known as cold junction and is used to maintain electronic components at a desired temperature. The hot junction is cooled by using active or passive heat sinks. The reason for their limited usage is because they are always used in conjunction with other cooling techniques as the hot junction of thermoelectric cooler needs to be cooled. However, this method is highly effective in some limited cases where the temperature of surroundings is higher than temperature margin required for reliable performance of electronic components. In such cases, cold junction can be used to cool electronics to maintain temperature below a certain margin. Subsequently hot junction can operate at temperature higher than the ambient temperature.

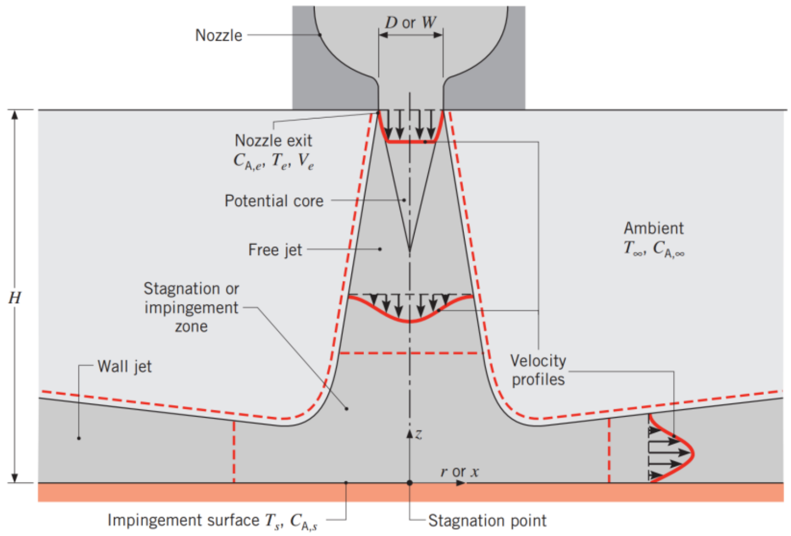

Figure 1.3: Jet impingement on a flat surface (adopted from Fundamentals of heat and mass transfer - Incorporate & Dewitt 7th edition)

Jet impingement is used for cooling high power density electronics which have a higher demand for cooling. Jet impingement cooling of electronics involves impinging a jet (of working fluid) onto surface in contact with a heat source. There are mainly two types of jet impingement, free-surface jet, which uses a dense fluid in a less dense medium such as air, submerged jet, where a jet impinges in a medium of same fluid as the jet. It has been shown that submerged jet impingement has a higher heat transfer coefficient than free jet for $Re > 4000$ [3]. The fluid leaving nozzle or jet is usually turbulent and the flow in wall jet region consist of vortices that aid in heat removal from contact surface.

1.2 Review on Additive Manufacturing

Additive Manufacturing (AM) is a relatively new technology in the field of manufacturing which came into light a few decades ago. AM refers to building a 3D object by adding material layers upon layers unlike most of the conventional manufacturing methodologies which are subtractive in nature. Additive techniques enable designing and manufacturing parts with intricate internal geometries that were previously difficult to achieve with conventional techniques like machining and casting. Fused Deposition Modeling(FDM) which uses a continuous filament of thermoplastic material is the most common 3D printing technique. AM techniques for crafting metal parts using amorphous powders are on the rise with some of them even producing industrial grade components [4]. Metallic components produced using AM techniques like Selective Laser Sintering(SLS) and Direct Metal Laser Sintering (DMLS) have different mechanical properties, residual porosity, and surface roughness from the original metal powder. This is closely related to the complex mechanisms involved in heat adsorption and transmission of powders and in melting and consolidation of powders [5]. The process of melting and refusing itself creates inherent microstructures that are different from parent material. There have been many studies characterizing the microstructures of materials produced using SLS and DMLS [6-7].

1.3 Present Work and Objectives

Jet impingement has been established as an efficient cooling method over the past few decades. Jet impingement onto additively manufactured target plates is a widely studied topic. Additive manufacturing methods use various binding techniques like Solid State Sintering (SSS), liquid phase sintering (partial melting) or full melting. The outcome of each of these techniques exhibit certain deformations related to operating conditions [8]. DMLS was used to manufacture target plates used in the current study and it falls under liquid phase melting. The most common deformation observed in this technique occurs when a laser melts and fuses a few more undesired powder particles together due to either a long exposure time or a lack of resolution. This is termed as warpage and was prevalent in the sample manufactured in the form of interconnections between cylindrical pin fins. In this study, the effects of such surface imperfections associated with DMLS are discussed in the light of jet impingement heat transfer. The aforementioned interconnections were characterized, and a more accurate geometry was reconstructed from the data. Numerical analysis using actual geometry resulted in a better prediction of heat transfer than intended geometry. This method of characterizing AM samples are key to understanding effects of surface imperfections on thermal hydraulic performance. Numerical models that inculcate surface topology post manufacturing are thus more accurate than numerical models that solely use intended design.

This document has been structured to discuss in detail the work carried out to understand the effects of surface imperfections with help of numerical models. Numerical model of an actual geometry of a 3D printed metal target surface was compared with results from the numerical model intended geometry. A brief description of content of each chapter is as follows:

Chapter 1 presents a basic introduction to the current technologies used for cooling electronics and a review on additive manufacturing techniques.

Chapter2 consists of literature survey on the methods additive manufacturing, studies on additively manufactured target plates under impinging jet, jet-to-target, and jet-to-jet configurations, etc.

Chapter 3 comprises of a detailed description of the experimental setup, the defects in AM process, surface roughness measurement and profilometry.

Chapter 4 presents the computational domain, geometries, grid independence study, spanwise grid convergence, numerical solver and boundary conditions used.

Chapter 5 explains the results obtained from experiments and the numerical analysis. A comprehensive study on heat transfer coefficient, velocity and pin fin effectiveness is presented.

CHAPTER 2

LITERATURE SURVEY

Advancements in the field of additive manufacturing(AM) are revolutionizing the world of science and technology slowly and steadily. Methods like Selective Laser Sintering (SLS) and its metal-based counterpart, Direct Metal Laser Sintering (DMLS) are capable of producing components that would otherwise seem impossible to manufacture using conventional techniques. Together with the ease of manufacturing, additively manufactured products exhibit a higher yield strength compared to similar products manufactured conventionally. **Manfredi et al.** [7] characterized AlSiMg alloy processed by DMLS and observed mechanical properties of AM alloys to conventional alloys. An augmentation in yield strength of 40% compared to similar aluminum alloys was reported. This is due to very fine microstructures closely related to complex heating and cooling cycles of additive process. A comprehensive review on different methods of metal AM, benefits of AM and the technological challenges of AM can be found in [9].

Simchi and Pohl [10,11] studied the effects of processing parameters of DMLS such as laser power, scan rate, thickness of layer and scanning geometry on the microstructural features of an iron-based powder. DMLS offers a wide range of possibilities to be exploited in the field of heat transfer. Employing additively manufactured components can enhance heat removal rates and boosts the efficiency of heat transfer components [12]. Additively manufactured products have innate roughness which naturally increases heat transfer rate. Roughness effects on fluid flow and heat transfer characteristics in micro channels processed by DMLS have been extensively studied by **Stimpson et al.** [13]. **Raghavan** [14] examined various numerical models to capture the difference in heat transfer and fluid flow in a laser welding model to a direct metal depositing AM process. A significant difference in penetration depths and volumes even for similar geometries was reported.

AM process can also be exploited for combining several components as one and that can collectively enhance thermal and hydrodynamic performance [15]. **Ventola et al.** [16] investigated the effects of roughness elements manufactured using DMLS on heat transfer for electronics cooling. It was observed that heat transfer close to wall was dominated by eddies with size depending on the roughness dimensions and viscous (Kolmogorov) length scale. An earlier study on optimal combination of random roughness features to maximize internal cooling performance by **Snyder and Thole** [17] showed that increasing friction factor resulted in a rise in Nusselt number of the cooling channels for small hydraulic diameters. But the augmentation of Nusselt number did not increase proportionally with the augmentation of friction factor. **Kirsch and Thole** [18,19] isolated the effects of surface roughness versus wall shape in numerically optimized additively manufactured micro cooling channels. Roughness is not the only factor augmenting heat transfer characteristics. Components processed by DMLS or any AM process have a relatively higher surface area due to the fine microstructures that are often more porous than their conventionally manufactured counterparts.

Dupuis et al. [20-22] characterized the enhancement in thermal and hydraulic performance of pin fin arrays produced using cold spray AM and concluded that convective heat transfer coefficient correlated better with turbulence intensity than turbulent kinetic energy. A similar study including pyramid shaped pin fins with flow structure identification and analysis can be found in [23]. **Ferster** [24] studied the effects of geometry, spacing of pin fins in additively manufactured microchannel pin fin arrays. Cylindrical, triangular, star shaped, and dimpled spherical pin fins were studied. It was concluded that additively manufactured triangles and cylinders perform better than conventional pin fin array. There was a visible difference between designed and manufactured pin fins. A cross sectional view of the pin fins can be seen in Figure **2.1**.

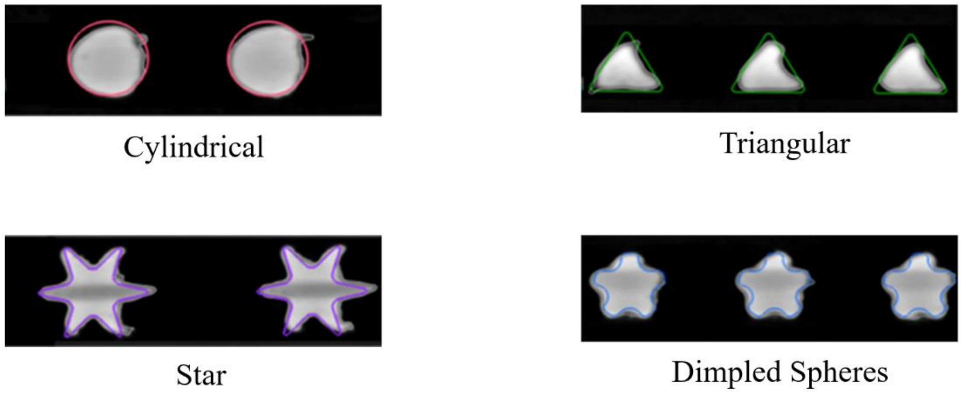

Figure 2.1: Intended vs Actual shape of pin fins manufactured using DMLS (picture adopted from **Ferster** [24])

Jet impingement is one of the most popular methods to cool components in high power-density electronics. Some of the early work on circular jet impingement without a cross flow can be found in **Goldstein** [25] and **Holger** [26]. **Zuckerman** [27,28] investigated various numerical models to characterize turbulence in a single jet impinging on a circular plate. $k - \omega$ was reported to be perform best in boundary layer flows such as wall-jet region. Employing an array of jets is known to be more effective at cooling, **Kercher and Tabakoff** [29] studied heat transfer by a square array of circular jets on a flat surface and reported a correlation between jet-to-target (Z/D_{jet}) spacing and Nusselt number. **Garimella** [30] concluded that local heat transfer coefficient increased with reduction in jet-to-target spacing with this effect being stronger at higher Reynolds numbers. Jet configurations also play a role in heat transfer as they facilitate crossflow under the jets.

San and Lai [31] studied the effects of jet-to-jet (X/D_{jet}) experimentally and showed that, above a critical X/D_{jet} an array of jets essentially behaved as single jets. **Yong et al.** [32] reported strongest jet impingement heat transfer of array of 5×5 jets is achieved for the case $X/D_{jet} = Y/D_{jet} = 3$. A variety of extended surfaces have been scrutinized over the years under the flag of jet impingement heat transfer. Study on effects of U-shaped cross flow diverters under an array of jets can be found in the literature [33]. **Singh et al.** [34] studied cylindrical, cubic, and concentric micro-roughness shapes of the order of $0.5 - 1.5\ mm$ under an array of jets and reported a $10 - 30\%$ increased fin effectiveness for cylindrical fins. **Sundaram** [35] explored different concentric shapes of additively manufactured pin fins and their effectiveness when subjected to array of impinging jets. The effect of pin-fin height, spacing and diameter under an array of 5×5 jets with an $X/D_{jet} = 3$ was also studied by **Sundaram** [35].

Dupuis et al. [21-22] studied truncated pyramidal pin fin arrays produced using Masked Cold Gas Dynamic Spraying (MCGDS) AM process in channel flow for $500 < Re < 2500$. It was found that manufactured pin fins deviated significantly from design intent. The profile along slant height of pyramidal pin fins was observed to be crooked at places. An Idealized model and a model with misaligned taper were numerically studied. The edges of pyramidal pin fins were observed to be rounded instead of a sharp shape opposed to idealized geometry. The main difference between ideal and actual geometry was the inherent roughness of pin fins attributing to microstructures as a result of AM process. This is clear from optical scans shown below in Figure **2.2**.

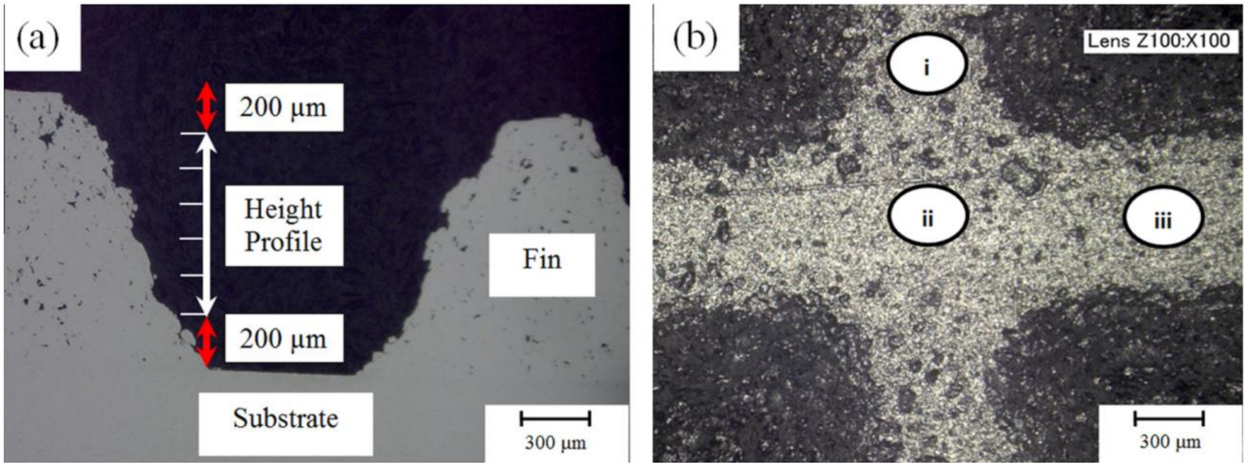

Figure 2.2: Surface imperfections incurred in pyramidal pin fins processed through cold spray method (picture adopted from **Dupuis et al.** [22])

This study concentrates on the effects of additively manufactured pin fins on local heat transfer coefficient under an array of impinging jets. Subsequently focusing on geometrical limitations incurred as a result of DMLS process. Experiments were carried out using two test coupons, one smooth and, the other with cylindrical pin fins that were manufactured from AlSiMg alloy and processed using DMLS method. Numerical analysis of smooth plate was a good match with experimental results presented in **Singh et al.** [34]. However, the same does not hold true for cylindrical pin finned target plate. When scrutinized carefully, it was evident that space between pin fins was not actually empty. The flow in channels between pin fins were obstructed by tiny interconnections between pin fins. These interconnections are a natural deterrent to crossflow, limiting the rates of heat removal from test coupon. The test coupon was scanned using a laser scanning microscope and interconnections were characterized using profilometry. A modified geometry was reconstructed from the data on interconnections. This new geometry was used for numerical analysis to better understand the actual behavior of test coupon. Numerical analysis of modified geometry proved to be a better match with experimental results than intended geometry.

CHAPTER 3

EXPERIMENTAL PROCEDURE AND ADDITIVE MANUFACTURING

3.1 Experimental Setup:

The schematic of experimental setup is shown in Figure **3.1**. Air was used as the working fluid. Compressed air at a pressure of 120 psi was drawn from a compressor located outside the building. Compressed air was then passed through a buffer tank, located in close proximity of the experimental set up. Buffer tank was used to provide a constant supply devoid of any pressure fluctuations from main supply. A pressure regulator and a 2-way gate valve were installed downstream of buffer tank to regulate the pressure and flow rate, respectively. The rate of flow was measured in g/s using an orifice meter by measuring differential pressure across the orifice. Dwyer $607-9, 0-25$ inwc differential pressure transducer was used for differential pressure measurement. An entry length of 35 times the hydraulic diameter(D_h) and an exit length of 10 times D_h was provided to ensure proper flow rate measurement. Test section was checked thoroughly for any leaks before the experiments.

A plenum of square cross section made of plexi glass was used for experiments. The D_h of plenum is same as the side length of plenum as cross section is a square and is equal to $50.8\ mm$. A divergent diffuser was used for a smooth flow transition from a circular tube to the square plenum made of plexi glass. Plenum was designed to accommodate $10\ D_h$ of length before jet plate to ensure the flow is hydrodynamically fully developed before reaching jet plate. Experiments were conducted for Reynolds number ($Re_{D_{jet}}$) of $3000, 6000, 9000$, and 12000. The static pressure was measured upstream of orifice meter using Omega $PX319$, $0-30$ psig pressure gauge to calculate power required to maintain the desired Reynolds number across the test configuration. A J-type thermocouple was used for temperature measurement right before the plenum and after orifice meter.

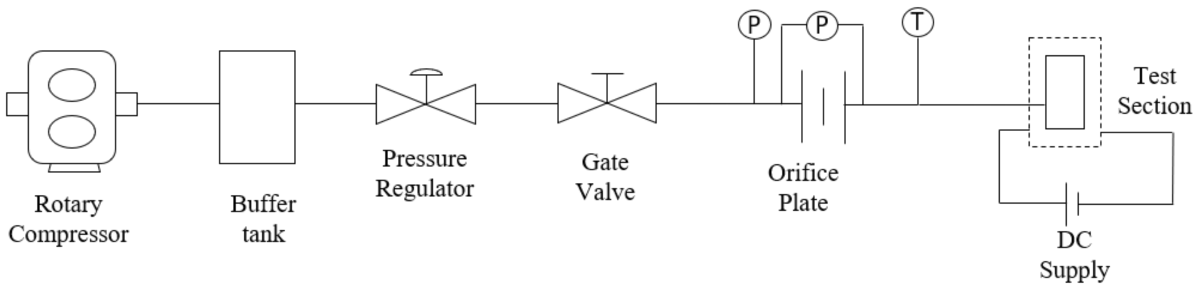

Figure 3.1: Schematic of the experimental setup

A schematic of heat source, target plate, insulation and location of thermocouples has been shown in Figure **3.2**. As discussed earlier, the two test coupons of cross-section area 2×2 inches were made of AlSi10Mg alloy with a thermal conductivity of $119\ W/mK$. A patch heater of 2×2 inch dimensions was attached to the bottom of target plate using a highly conductive thermal grease with a thermal conductivity of $2.31\ W/mk$. Four holes were drilled on test coupons to insert k- type thermocouples for temperature measurement at the center of each quadrant. Fiberglas was glued to the set up below heater to provide insulation to avoid any heat loss from heater to ambience from below. A DC power source was used to provide uniform heat flux to target surface. All the thermocouples, pressure gauges and differential pressure measurement devices were connected to a Data Acquisition System(DAQ) for constant monitoring.

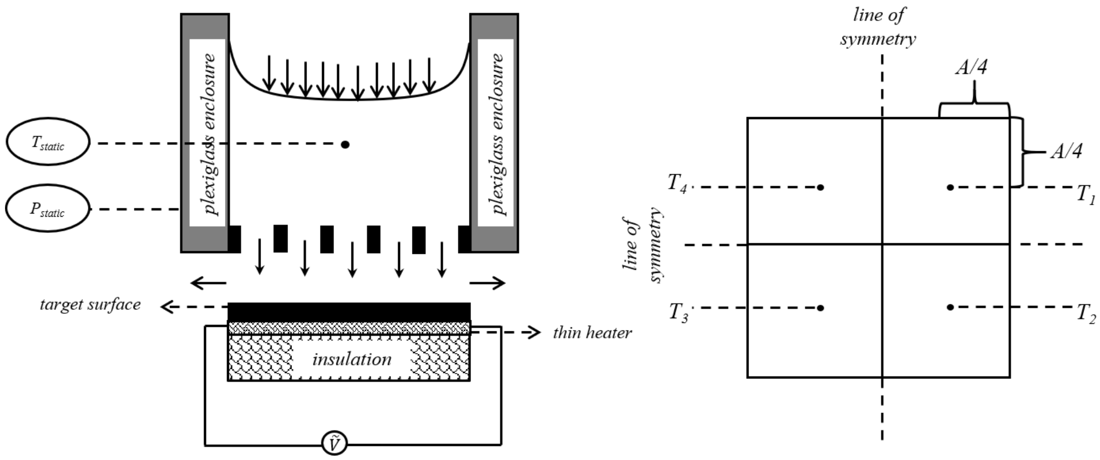

Figure 3.2: The target plate assembly (left) with heat source and insulation, location of surface thermocouples to measure average wall temperature (right)

3.2 Description of test configuration

3.2.1 Target plate configuration

The two different test coupons that were used for experiments are smooth target plate and target plate with cylindrical pin fins which is referred as cylindrical target plate or test coupon. Each test coupon is $50.8\ mm$ long, $50.8\ mm$ wide, and base height is $3.175\ mm$. The smooth test coupon is manufactured by DMLS, but the top surface is not polished and thus is inherently rough, but there was no artificial roughness added to plate like the finned test coupon. The test coupon with cylindrical micro pin fins was processed through DMLS to print micro pin fins of diameter and height $D = H = \ 500\ \mu m$. Distance between micro pin fins was $S = \ 700\ \mu m$. The cylindrical test coupon is shown in Figure **3.3**.

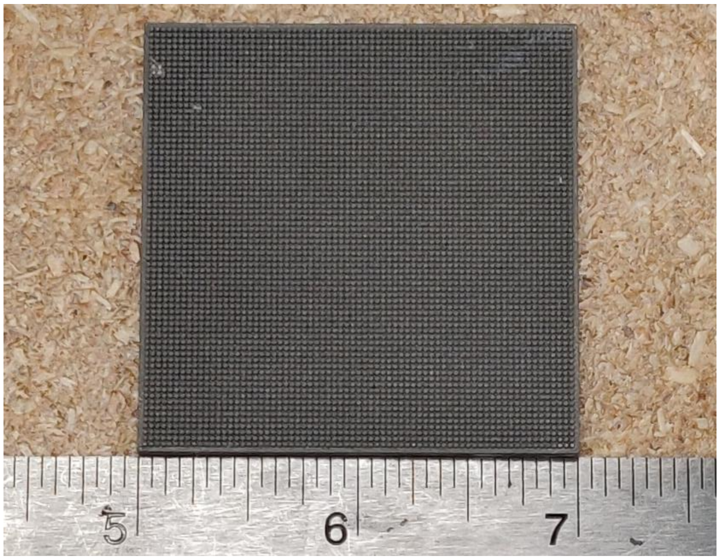

Figure 3.3: Target plate with cylindrical pin fins as manufactured

As shown in the Figure **3.2**, whole domain can be split into four equal quadrants. SEM images were taken to closely observe the actual geometry of test coupon. Tiny grain like interconnections can be seen between cylindrical micro pin fins in Figure **3.4**. These interconnections are a result of warping of laser around roughness elements. The geometry consists of micro pin fins with a diameter of 500 microns and center to center distance of micro pin fins is 700 microns. Such extreme distances has pushed the limits of DMLS manufacturing. Actual and intended geometries of the cylindrical micro pin finned test coupon as assessed using the SEM images and are given in Table **3.1**.

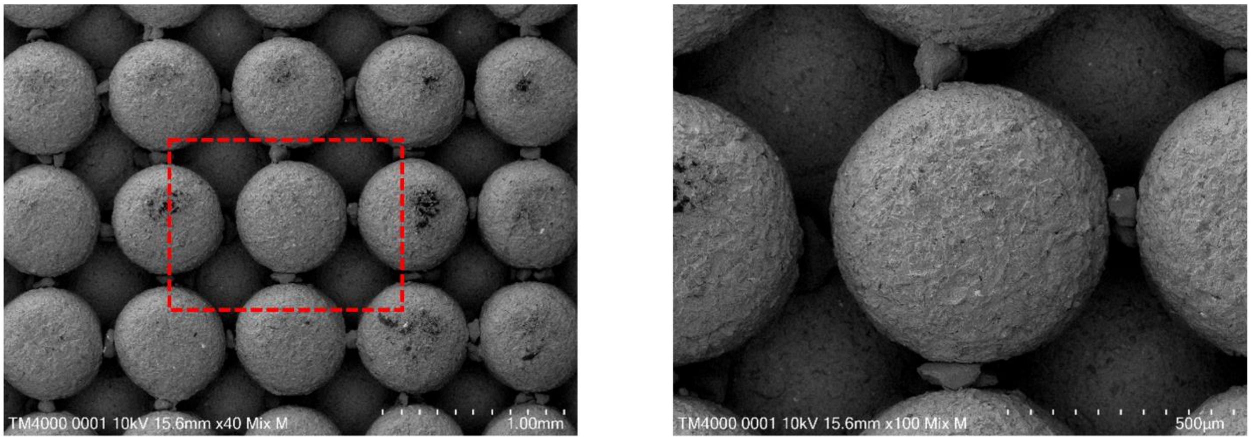

Figure 3.4: Scanning Electron Microscope (SEM) images of the test coupon

Table 3.1: Actual and Intended dimensions of the target plate

Dimension	Diameter in μm (D)	Space between pin fins in μm (S)	Interconnection thickness in μm
Actual	617	702	101.3
Intended	500	700	0
Deviation	23.4%	0.29%	NA

3.2.2 Jet plate configuration

An array of 5×5 jets was used with a jet diameter $D_{jet} = 3.3867\ mm$. The jet-to-jet spacing was set to be same in the spanwise and streamwise direction. Jet-to-Jet spacing of $X/D_{jet} = Y/D_{jet} = 3$ was used for the maximum cross flow as mentioned in **Yong et al.** [32]. The jet plate with a thickness of $4D_{jet}$, where D_{jet} is the diameter of nozzle was used. A drawing of jet plate can be found in Figure **3.5**. Jet-to-target spacing was set to be equal to $Z/D_{jet} = 1$ as suggested by **Singh** [34].

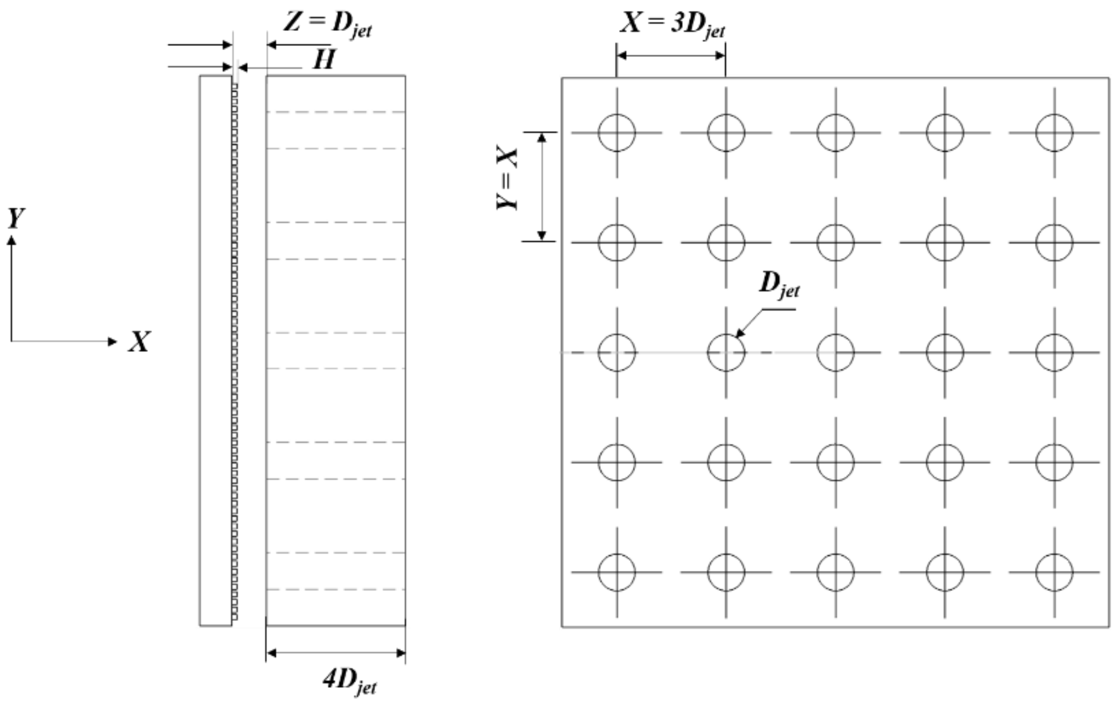

Figure 3.5: Jet plate Configuration

3.3 Experimental Heat Transfer Coefficient (HTC) Calculation

A constant voltage supply was supplied to a patch heater attached to test coupon. The total heat supplied (q_{total}) was calculated using voltage drop across the heater. Heat loss due to conduction, radiation was calculated by cutting off the air supply and was found to be negligible compared to total heat flux input. Heat loss due to natural convection was also found to be negligible for Reynolds numbers greater than 3000 and for a nominal temperature difference of $20°C$. The average of wall temperature measured by four k-type thermocouples embedded into the test surface as shown in Figure **3.2** was used for HTC calculations. Equation (1) was used for evaluating averaged convective heat transfer coefficient, where T_w represents the steady state wall temperature and T_{aw} stands for temperature of mainstream far from test coupon. Only the base surface area of test coupon excluding the extra surface are of micro pin fins was considered for calculation.

$$\bar{h} = \frac{q_{conv}}{A_{smooth}(T_w - T_{aw})} = \frac{q''_{total} - q''_{loss}}{(T_w - T_{aw})} \tag{1}$$

The HTC at wall calculated from equation (1) is an average value and does not provide insights into local HTC characteristics. Area averaged HTC from above equation was used to calculate non-dimensional heat transfer coefficient Nusselt number (Nu). Nusselt number was calculated using equation (2). Thermophysical properties of air were calculated at film temperature which is an average of temperatures of test coupon and the flow entering plenum.

$$Nu = \frac{\bar{h}D_{jet}}{k_f} \tag{2}$$

3.4 Additive Manufacturing(AM) process

Additive manufacturing has been around for almost four to five decades now, but due to certain patent laws and legal issues many techniques came into light only two decades ago. However, as soon as the concept of AM came into light, industries around the world quickly adapted and revolutionized the field of rapid prototyping. In the present study, DMLS was used to manufacture target plates and thus is focus of the discussion. DMLS uses a laser that is concentrated on a bed containing powdered metal or alloy to bind particles into small solid structures. The parts and products manufactured through this process exhibit better physical properties due to fine microstructures and continuity of material throughout the part. Materials processed through AM undergo complex thermal processing cycles. Very little is known about the microstructures formed during the AM process and a lot is yet to be unfolded in the field of AM. Aluminum alloy AlSi10Mg was chosen for experiments as AlSi10Mg exists as a fine amorphous powder in its natural state and is lightweight. Mechanical properties of DMLS processed AlSi10Mg alloy is a widely studied topic. Important literature regarding the characterization of mechanical properties of DMLS processed AlSi10Mg can be found in **Manfredi et al.** [7]. Processing parameters such as laser power, thickness of layer, scan time and rate etc. play an important role in mechanical and thermal properties of the parts produced.

3.4.1 Defects in Additive Manufacturing

Additive Manufacturing is a convenient process as any component can be manufactured with just a CAD model. This gives AM a huge advantage over conventional manufacturing techniques which often require two or more than two process in conjunction like CNC machining, foundry, welding, casting etc. This saves a lot of time and resources and thus AM is commonly referred as “Rapid Prototyping”. But AM techniques come with inherent defects, one of which is discussed by **Ventola** [16]. During AM process such as DMLS, 3D object is generated from a CAD model by adding layers on top of one another. So, the contour of a DMLS manufactured component is a stepped approximation of the shape of intended CAD model. As a result of this, all parts manufactured by AM processes exhibit a staircase effect.

Build direction (k) directly influences the scope of staircase effect that appears mainly along inclined planes and curved surfaces. The inclination angle (ϑ) is defined as the angle between build direction and normal (n) to the layer face. If the inclination angle is decreased or the layer thickness is increased, stair-effect becomes more evident. If the inclination angle is high, staircase effect is reduced, and surfaces will be smoother. The error related to staircase effect can be computed by studying cusp height which is the maximum distance between intended geometry boundary and boundary of a component produced by DMLS. Staircase effect is the topic of interest of several researchers in AM industry. Ideally intended geometry of cylindrical pin fins should have been an easier shape to manufacture. Yet staircase effect is clearly visible in the component as the top surface is spherical rather than being flat.

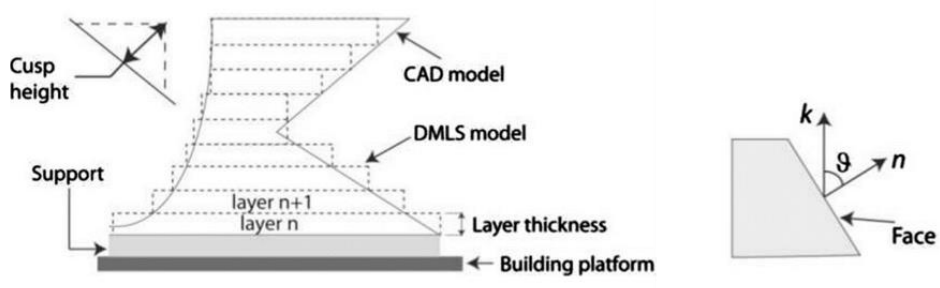

Figure 3.6: Staircase effect (Figure adopted from **Ventola** [16])

3.4.2 Surface roughness measurement

Roughness is typically considered to be the high frequency, short wavelength component of the measured surface. It can be quantified using waviness profile with a varying wavelength. Test coupon with cylindrical micro pin fins was scanned using a "Keyence confocal laser microscope" in order to capture line and surface roughness details. The software Keyence Multi-file Analyzer was used for determining the profile of micro roughness features. A 3D view of test coupon showing cylindrical micro pin fins and interconnections can be seen in Figure **3.7**. In addition to the interconnections, there are also troughs between pin fins, clearly visible in blue color in figures. These troughs also affect roughness calculations along with the interconnections.

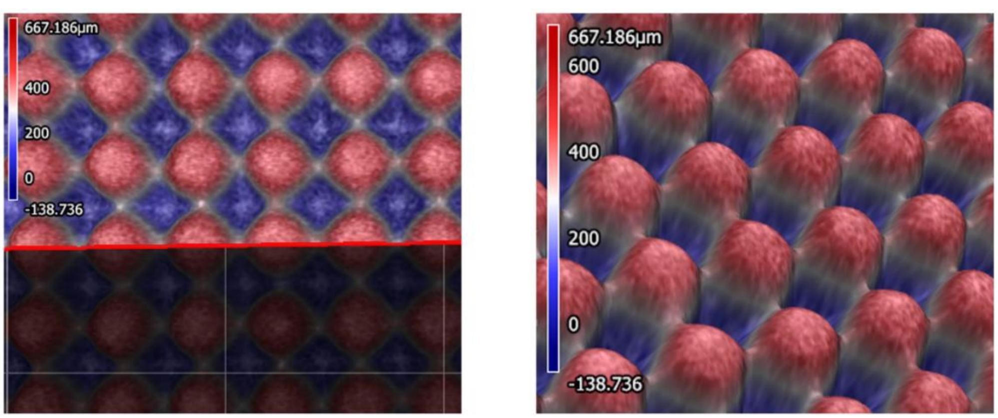

Figure 3.7: Orthogonal (left) and Isometric (right) views of the cylindrical micro pin fins and the interconnections generated by using the information from a confocal laser microscope

It is clear from Figure **3.7** that even the cylindrical pin fins are not entirely cylindrical. The top of pin fins is curved like a sphere instead of being flat as intended in design. The line roughness variables were measured along 30 parallel lines with a distance of $350\,\mu m$ between each line. While measuring the roughness, it was ensured that both micro pin fins and interconnections are amply covered to avoid any biases. The values of roughness variables were then averaged over all the 30 lines. A total of three line roughness variables were considered for the study namely arithmetic mean roughness height (Ra), maximum roughness height (Rz) and root mean square roughness height (Rq).

$$Ra = \frac{1}{l_r}\int_0^{l_r} |z(x)|dx \tag{3}$$

$$Rz = \frac{\sum_{i=1}^{n} Rz_i}{n}, Rz_i = Rp_i + Rv_i \tag{4}$$

$$Rp_i = \max z(x)\,;\ Rv_i = |\min z(x)| \tag{5}$$

$$Rq = \sqrt{\frac{1}{l_r}\int_0^{l_r} z^2(x)dx} \tag{6}$$

Where Δ_i is 5^{th} order Savitzky-Golay smoothing filter, Rp_i and Rv_i are the i^{th} highest peak and lowest valley, respectively. l_r is length of line, z(x) is height along line. The table below shows the values of averaged line roughness variables along different set of lines. The line roughness variables of intended geometry are also calculated for comparison. The difference between the average value of line roughness Ra of both intended and actual profiles is about 25%. But Ra itself is does not cover the whole story of roughness. As the height of reference line itself is prone to accommodate interconnections and troughs. Hence, root mean square height Rq is a better indicator of roughness and notably the difference is almost 50%. This confirms that actual component generated by DMLS process is very rough.

Table 3.2: Line Roughness variables

Line roughness variables	Ra (μm)	Rz (μm)	Rq (μm)
Average height	113.99	502.11	130.60
Intended Average height	150.59	500	274.40
Maximum height	153.23	624.52	172.90
Minimum height	65.84	381.68	79.48
Standard Deviation	28.319	58.179	29.280

To better understand the roughness connected to AM process, surface area roughness was also studied. Extension of the above mentioned line roughness variables to a surface instead of a line generates 3 more area roughness variables. Arithmetic mean height (Sa), maximum roughness height (Sz) and root mean square height (Sq) are evaluated across the entire scanned region. The values of area roughness variables are attached in the table below. A similar trend to that of line roughness can also be observed with area roughness variables. The difference in average height between actual and intended profiles is only about 15%. But the difference in root mean square height is a staggering 40%. Hence the results of area roughness calculations are in good agreement with the line roughness calculations.

Table 3.3: Area roughness variables

Area roughness variables	Sa (μm)	Sz (μm)	Sq (μm)
Average height	163.11	805.92	190.17
Intended Average height	191.77	500	309.65

Material ratio curve of the line roughness and area roughness measurement are shown in Figure **3.8:** Material Ratio curve of the line roughness (left) and area roughness (right) measurement. It is clear from the probability density function of line roughness that the top surface of micro pin fins lies between $20\mu m$ to $100\mu m$ from the reference line ($0\ \mu m$). Whereas the intended geometry's reference line is aligned with top surface for line roughness calculations and bottom surface for area roughness calculations. Y axis in the material curve ratio is load length ratio which is obtained by dividing the total length of curve data exceeding the cut level by entire length.

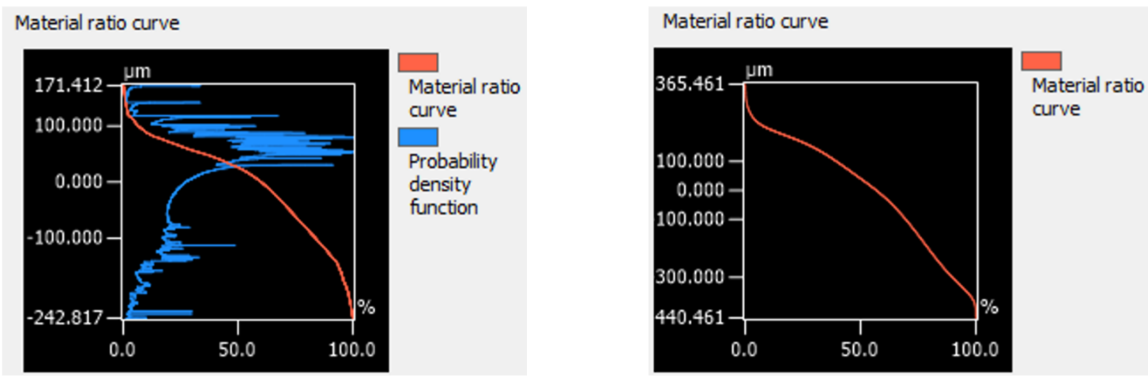

Figure 3.8: Material Ratio curve of the line roughness (left) and area roughness (right) measurement

3.4.3 Profilometry

Profilometry is a technique used to extract topographical data from a surface. This can be a single point, a line scan or even a full three-dimensional scan. The purpose of profilometry is to get surface topology, step heights and surface roughness. In this study, optical profilometry using a confocal laser scanning microscope was performed. The top left quarter of cylindrical test sample is scanned directly from above. Prior to the optical profilometry, computerized tomography (CT) scan was also considered to study the surface roughness. But data from CT scan was too high definition. CT scan also picks up volumetric features along with the surface features. The idea of CT scans was later scrapped due to insufficient computational resources. The optical scans were sufficient to produce a reliable numerical model. The profile of roughness was studied by averaging the profiles of all micro pin fins and interconnections aligned horizontally with pin fins and is show in Figure **3.9**. Intended profile is displayed in dotted red line and the actual profile is displayed in blue. Y axis is the height of micro pin fins in μm. It is clear from the figure that there is significant deviation in actual profile from the intended profile. Interconnections of almost $450\ \mu m$ can be noticed between the pin fins.

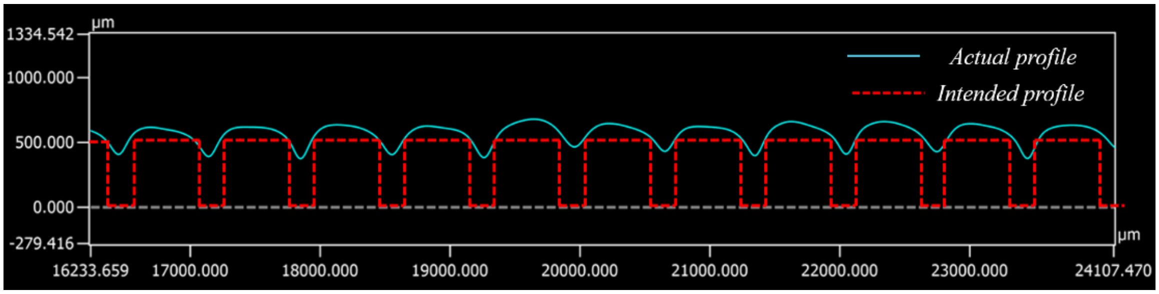

Figure 3.9: Actual and intended profiles of the cylindrical micro pin fins

CHAPTER 4

NUMERICAL MODELLING

4.1 Geometry of Computational Domain

A total of 5 geometries were used for numerical modelling. The first model is a smooth target plate $50.8\,mm \times 50.8\,mm$ wide and $3.175\,mm$ thick. Geometry representing the design intent of target plate with cylindrical micro pin fins is referred as intended geometry. The modified geometry representing the actual final product manufactured using DMLS is referred as actual geometry. In addition to these three models, two more models were studied. One depicting a target plate with truncated pyramidal pin fins of design intent and another an approximation of what the actual target plate might look like post manufacturing. As discussed earlier, due to symmetry only top left quarter domain was used for computation and is shown in Figure **4.1**. The quarter domain split by the planes of symmetry enclose four full jets, four half jets and a quarter jet amounting to 6.25 jets in total. There are a total of 35.5×35.5 pin fins in the computational domain.

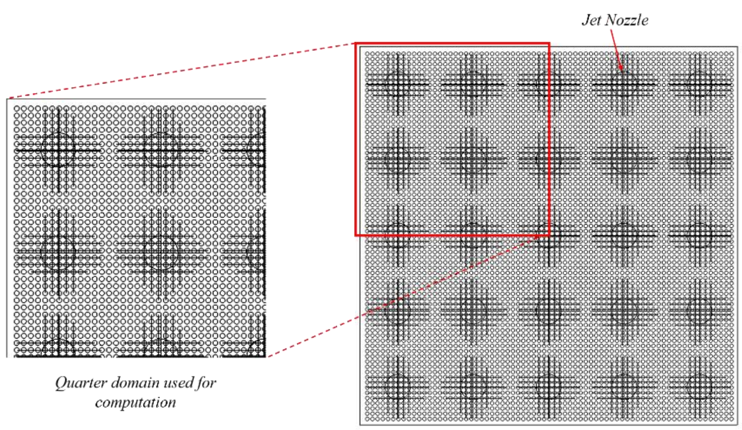

Figure 4.1: Quarter domain used for computational domain with 6.25 jets

The actual geometry is generated using data obtained from the profilometry discussed in section 3. The profile of interconnections was averaged over 33 lines with a distance of $700\,\mu m$ between the lines. The resultant curve is then smoothed out using a gaussian filter. This profile is extruded both in X and Y directions across the smooth top surface of target plate. From Figure **3.7** it is clear that top surface of micro pin fins is not flat. Hence, they are filleted out to a spherical shape to better represent the actual shape of pin fins. Both the intended and actual geometries are shown in Figure **4.2**, difference between both models is clearly visible. To achieve satisfactory results the actual geometry was altered multiple times with different profiles and different fillet radii.

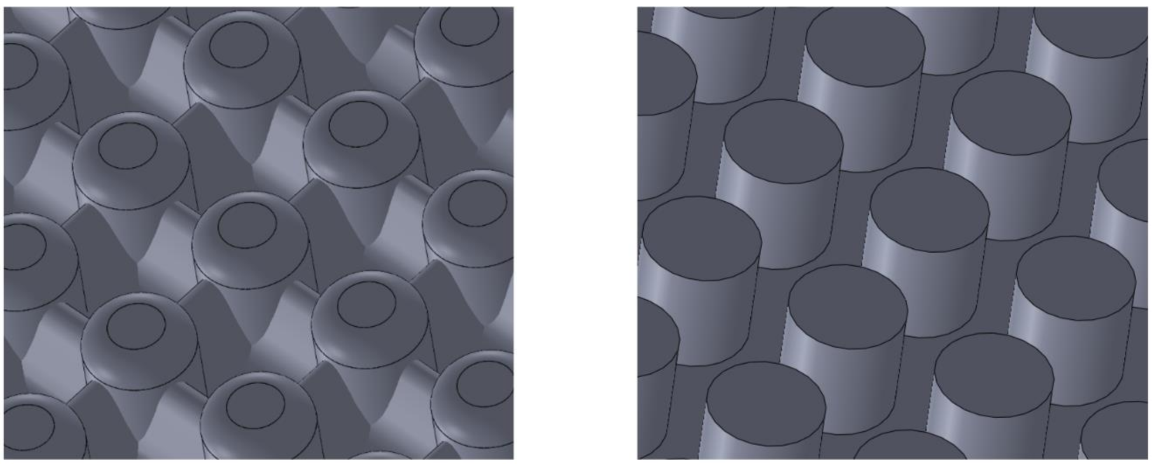

Figure 4.2: Geometry of the Actual (left) and Intended (right) cylindrical pin fins used for numerical modelling

The two models consisting of pyramidal pin fins are referred as Pyr_intended and Pyr_actual and are shown in Figure **4.3**. The height of pyramidal pin fins is 1mm with a base length of 1.5 mm and a top length of 0.5 mm. The dimensions of base plate were kept same as that of smooth and cylindrical target plates. The pyramid used for modelling is a right pyramid. The center to center distance between the pin fins is 2 mm. **Dupuis et al.** [21,22] and **Cormier** [23] studied pyramidal pin fins manufactured through cold spray AM technique. It was reported that, final product was inherently rougher than expected. The slant height of pyramids was found to be crooked, tilting in one direction. Considering all these surface imperfections, it is not difficult to assess that actual geometry after DMLS will also vary significantly. But for simplicity, in this study the actual geometry was generated by altering only the sharp edges. Fillets of 0.3 mm radius on top, sides and bottom edges were used to model the actual geometry.

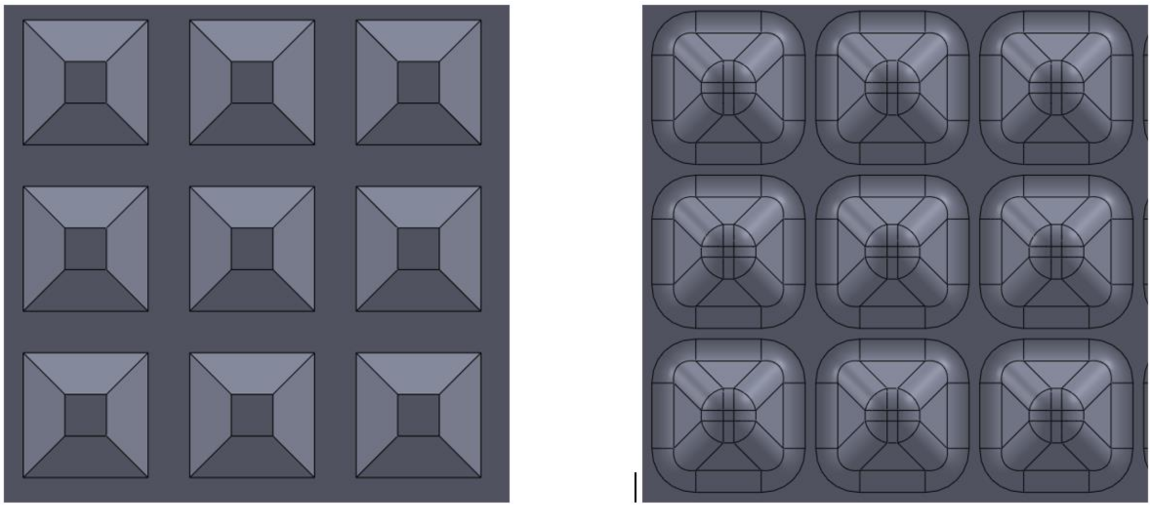

Figure 4.3: Intended (left) and Actual (right) pyramidal pin fins used in numerical modelling

4.2 Computational Mesh and Grid Independence Study

4.2.1 Computational Mesh

Grids play an equal and important role as the numerical solver, in producing precise results. Meshing was done using Ansys Meshing software to generate an unstructured conformal mesh. The mesh was mainly composed of tetrahedral elements in the bulk of fluid and solid domain. The boundaries contained few hexahedral elements. The $y+$ value was varied from 1.3 to 0.7 in smooth case and 0.7 to 0.5 for cylindrical case. Such a low value of $y+$ was necessary for numerical study to capture the flow physics at solid fluid interface.

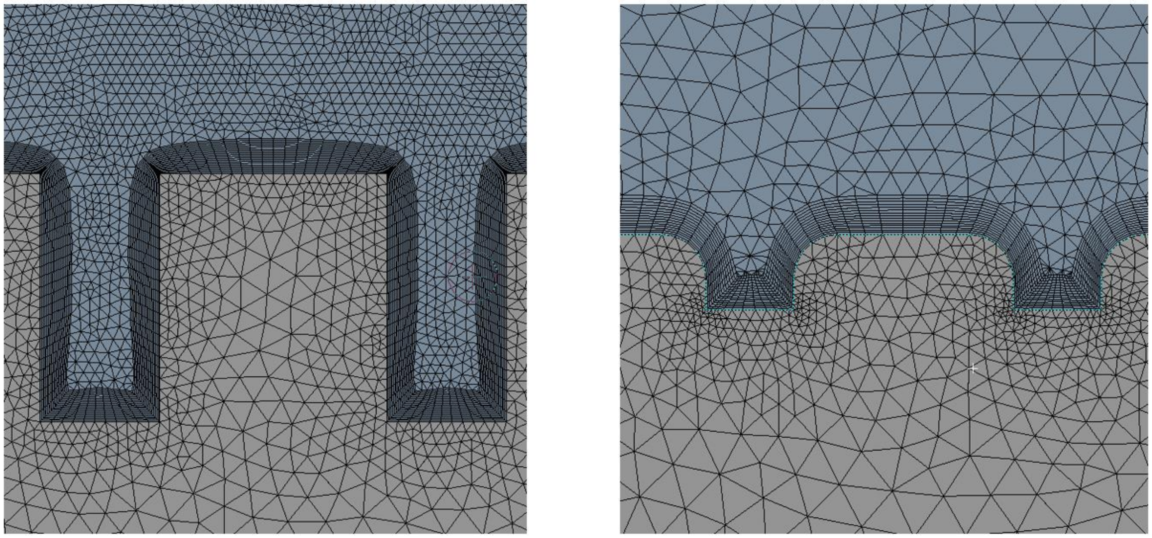

Figure 4.4: Grids used for the intended (left) and actual (right) numerical models

4.2.2 Grid Independence Study

Discretization error of numerical solution can be understood by examining the spatial convergence of solution. As the grid is refined, spatial discretization errors should asymptotically approach zero. The solution is then said to have achieved grid independence. That is further refining the grid is not desired as the computational power increases exponentially over an insignificant change in accuracy of results. It should be noted that numerical result which approaches an asymptotic numerical value is not the same as true physical solution. When solving many numerical models with a similar set of geometries it is suggested to carry out a grid independent study and follow a certain grid convergence index (GCI). This can reduce the burden of checking all grids for convergence separately. In this study four types of geometries were simulated using ANSYS solver. Hence, a grid convergence index was chosen by performing a grid refinement of study on both smooth and intended cylindrical grids.

Three levels of grids coarse, medium, and fine were generated varying the spatial discretization in the area of interest. Area of interest consists of target plate in solid domain and the space in fluid domain above target plate and below jet wall where jet impinges on target plate. The grid is refined by varying element sizes in target plate and fluid region beneath the jet wall. A parameter (h) that is an average of element size in both of these regions is considered for evaluating the grid refinement ratio (r). To avoid any inconsistencies in grid independence study, grid refinement ratio was maintained at a constant value of $r = 1.14$ for smooth case and 1.2 for cylindrical case.

4.2.3 Grid Convergence Index

Grid Convergence Index (GCI) is a measure of how far the computational value is from the asymptotic numerical value. A small value of GCI represents that the numerical solution is within asymptotic range. GCI was calculated using Richardson's extrapolation and equations used for the same are described below. The order of convergence is denoted by p and can be obtained from the slope of curve log(E) vs log(h), where E is the fractional error. A more direct evaluation of p can be obtained from the three solutions using a constant grid refinement ratio r. F_s is the factor of safety and is considered as $F_s = 1.25$ for over three or more grids. $f_{h=0}$ is an estimate of function value f in the limit of grid spacing goes to 0. f_1, f_2, and f_3 are the function values of numerical solution for the three grids studied that is coarse, medium, and fine, respectively.

$$p = \ln\left(\frac{f_3 - f_2}{f_2 - f_1}\right) / \ln(r) \tag{7}$$

$$E = \frac{\varepsilon}{r^p - 1}\ ; r = \frac{h_2}{h_1};\ \varepsilon = \frac{f_2 - f_1}{f_1} \tag{8}$$

$$f_{h=0} \cong f_1 + \frac{f_1 - f_2}{(r^p - 1)} \tag{9}$$

$$GCI_{fine} = F_s \frac{|\varepsilon|}{(r^p - 1)}; GCI_{23} = r^p GCI_{12} \tag{10}$$

The relative error ε should not be used as an error estimator. Hence E, the estimated fractional error was used to evaluate grid convergence. Non-dimensional heat transfer coefficient Nusselt number (Nu) was considered as function value. Table **4.1** and Table **4.2** shows grid spacings chosen for the grid independence study for both smooth and cylindrical case. The resultant GCI is close to 1 with a 0.12% error in smooth case and 6% in cylindrical case. Though GCI for cylindrical case is a bit high, the fractional error E between grids was only 0.7%. Hence the solution is assumed to have reached grid independence.

Table 4.1: Grid Independence study of smooth target plate case

Grid	No: nodes in million	$y+$	h	$r = h2/h1$	function value(f) = Nu	Deviation (%)
Coarse	7.64	1.3	6.08	1.00	47.5	0.63
Medium	11.0	1	5.33	1.14	47.4	0.83
Fine	16.4	0.7	4.69	1.14	47.8	0

Table 4.2: Grid Independence study of cylindrical pin finned target plate case

Grid	No: nodes in million	$y+$	h	$r = h2/h1$	function value(f) = Nu	Deviation (%)
Coarse	11.5	0.72	3.15	1.00	91.99	6.18
Medium	16.5	0.6	2.62	1.20	86.76	0.53
Fine	24.3	0.5	2.19	1.20	86.30	0

4.2.4 Spanwise grid convergence study

A spanwise grid convergence study for cylindrical and smooth case was also performed to critically assure the grid convergence. For the spanwise study, computational domain was split into 11 equal parts by 10 uniformly spaced vertical lines with a distance of $2.31\ mm$ between the lines. Numerical analysis was performed at $Re\ = 6000$ for all grids in the grid convergence study. Heat transfer coefficient was averaged across each line for three grids and is plotted against x axis. From the plot shown in Figure **4.5** it is clear that trends of peaks and valleys of HTC are closely matching in all three grids. Moreover, the average error of line averaged HTC values is 9% between medium and coarse grids and 3% between the fine and medium grids. As the lines are uniformly spaced, few lines fall directly under the jet region and other lie in space between the jets. This is visible from the plots as HTC is higher under jet (peaks) and lower elsewhere.

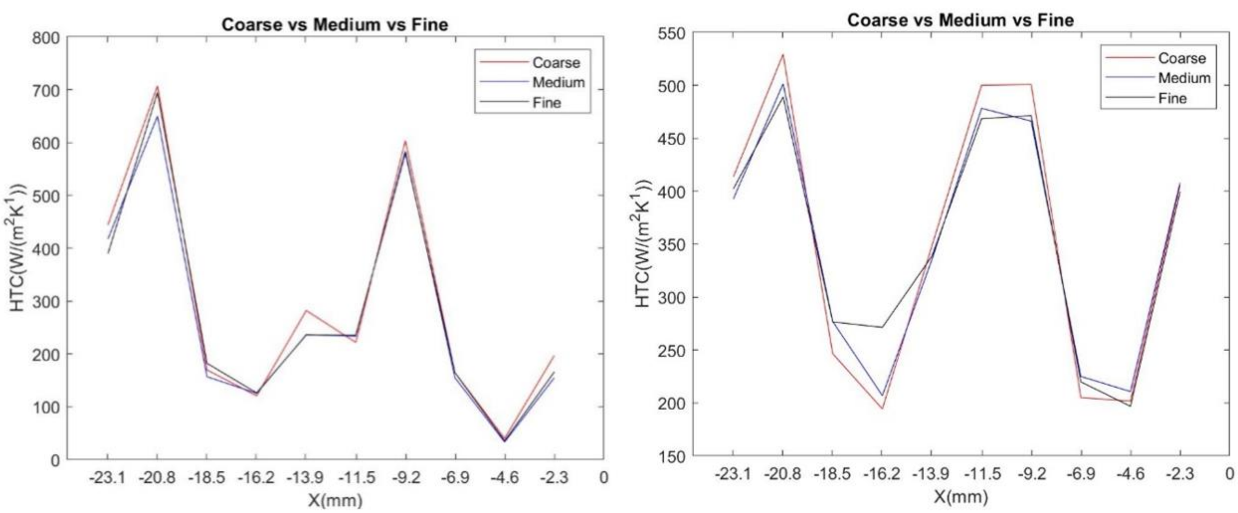

Figure 4.5: Comparison of line averaged heat transfer coefficient along the spanwise direction of three grids used for grid independence study. Smooth test coupon (right) cylindrical pin finned test coupon (left) at $Re\ =\ 6000$

4.3 Numerical Solver and Boundary Conditions

The steady state numerical analysis of jet impingement heat transfer onto additively manufactured cylindrical micro pin fins were done using finite-volume pressure-based solver in ANSYS Fluent 19.2. SIMPLE scheme was used to achieve pressure and velocity coupling.

Second-order upwind scheme was employed for spatial discretization of momentum, turbulence, and energy equations. Menter's Sheer Stress Transport(SST) k-ω model was employed for resolving turbulences in the flow. Similar numerical analysis of jet impingement heat transfer conducted by **Sundaram** [35] reported a good agreement between numerical and experimental results. The criteria for convergence was set as 10^{-5} for momentum equations and 10^{-8} for the energy equation. Numerical modelling of smooth target plate was carried out for the Reynolds numbers 3000 through 12000 and results were in good agreement with the literature [35].

The Boundary conditions used for numerical analysis are mentioned in Figure **4.6**. As discussed earlier, due to the symmetric nature of the whole domain, only a quarter domain was considered for all the numerical analysis. The inlet boundary condition was mass flow inlet which was varied to simulate flow at different Reynolds numbers from 3000 through 12000. The properties of air were calculated at the free stream temperature that is $295\ K$. The turbulent intensity at inlet was set as 5% with a turbulent length scale of 10% of hydraulic diameter D_h. A constant heat flux of $20kW/m^2$ was used as input at the bottom surface of test coupon. The top plate was coupled to bottom plate of test coupon thermally. This ensures even redistribution of heat flux throughout the volume of solid target plate from bottom surface. The outlet pressure is set as ambient pressure with a gauge pressure of 0 pascals. The four walls of solid domain excluding the top and bottom surface are given an adiabatic boundary condition. No slip, adiabatic boundary condition was used for boundaries of fluid domain excluding the symmetric regions like outer walls, jets, and jet wall.

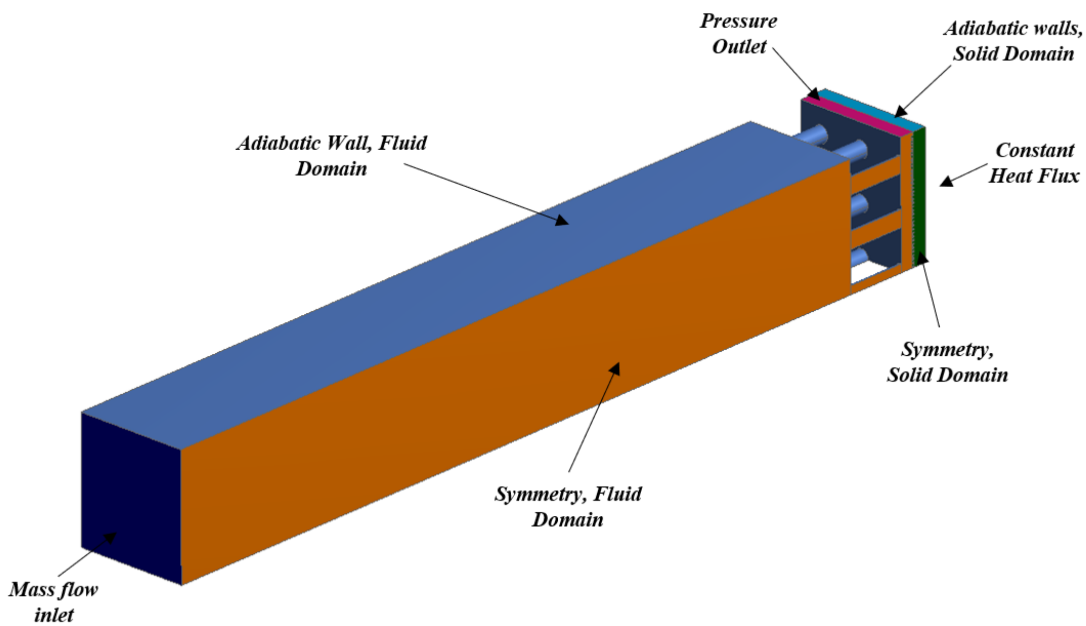

Figure 4.6: Domain used for numerical modelling and the Boundary conditions

4.4 Numerical Heat Transfer Coefficient Calculation

Numerical heat transfer coefficient was evaluated using equation (13). Where the local wall temperature at top surface of test coupon $T_w(x, y)$ including micro pin-fins was obtained as a function of (x, y) from solving conjugate heat transfer simulations. This temperature was substituted for T_w in the equation (1) earlier discussed in experimental HTC calculations. The convective heat flux as a function of (x, y) q_{conv} (x, y) is evaluated at top surface of target plate. Temperature of the mainstream flow was considered as ambient temperature for calculations. Heat transfer coefficient can be calculated using two different areas. The equation (12) described below uses A_{smooth} which is essentially the area of top surface of target plate without pin fins. The equation (13) uses A_{wetted} which includes the surface area of micro pin fins into account.

$$A_r = \frac{A_{wetted}}{A_{smooth}} \tag{11}$$

$$h_1(x,y) = \frac{q_{conv}(x,y)}{A_{smooth}(T_w(x,y) - T_{ambient})} \tag{12}$$

$$h_2(x,y) = \frac{q_{conv}(x,y)}{A_{wetted}(T_w(x,y) - T_{ambient})} \tag{13}$$

The non-dimensional heat transfer coefficient, Nusselt number is evaluated using equation (14) . Average heat transfer coefficient $\bar{h}$ was obtained by averaging $h_2(x,y)$ over the top surface of target plate. This average heat transfer coefficient was multiplied by area ratio and was used in equation(14) to evaluate the Nusselts number. The area ratio of cylindrical pin finned test coupon is 2.53 for intended case and 2.15 for actual case. The thermal conductivity of air k_f was calculated at the film temperature which is obtained by averaging wall temperature T_w and ambient temperature $T_{ambient}$. The Nusselt number obtained from $h_1(x,y)$ is not discussed as the results from $h_2(x,y)$ are in a good agreement with experimental results.

$$Nu = \frac{\bar{h}D_{jet}}{k_f} \tag{14}$$

Micro roughness elements increase the wetted surface area of target plate and thereby enhancing the rate of heat transfer. This is captured by studying the pin fin effectiveness of intended and actual cases of both cylindrical and pyramidal pin fins. Pin fin effectiveness was calculated from the numerical analysis by using equation(15). The heat transfer coefficient calculated from smooth and rough numerical models was used in conjunction with the surface area of models to evaluate effectiveness.

$$\varepsilon_f = \frac{q_{rough}}{q_{smooth}} = \frac{(hA)_{rough}\Delta T}{(hA)_{smooth}\Delta T} = \frac{(hA)_{rough}}{(hA)_{smooth}} \tag{15}$$

CHAPTER 5

RESULTS AND DISCUSSION

A comprehensive study of experimental and numerical results of area averaged and spanwise heat transfer coefficient, physics of flow and pin fin effectiveness are discussed in this section. The experimental non-dimensional heat transfer coefficient are validated with the results produced by **Singh et al.** [34]. A contrast between the results from intended and actual numerical analysis of cylindrical and pyramidal cases is presented in detail. Non-conjugate numerical analysis without the target plate was carried out to examine the feasibility of replacing conjugate numerical simulations. Finally, the coefficient of discharge, and pumping power characteristics of test section are reviewed.

5.1 Coefficient of Discharge

An array of 5×5 jets were used to supply coolant air to cool the target plate. Coefficient of Discharge (C_d) was evaluated experimentally by removing the target plate from test section and discharging air to ambient surroundings. Due to frictional losses across the test section especially through jets, the actual value of mass flow rate is lower than expected theoretical value. The variation in coefficient of discharge is studied as a function of plenum pressure ratio. A higher value of coefficient of discharge is an indicator of lower frictional losses and vice versa. Equation (16) which was used to evaluate the coefficient of discharge is given below. The plot of C_d vs Reynolds number is shown in Figure **5.1**. Coefficient of discharge was found to be consistent across the Reynolds numbers with a value of 0.8.

$$C_d = \frac{\dot{m}_j}{p_1 \times \left(\frac{p_2}{p_1}\right)^{\frac{\gamma+1}{2\gamma}} \left(\frac{\pi D_j^2}{4}\right) \sqrt{\frac{2\gamma}{(\gamma-1)RT_\infty}\left(\left(\frac{p_1}{p_2}\right)^{\frac{\gamma-1}{\gamma}} - 1\right)}} \tag{16}$$

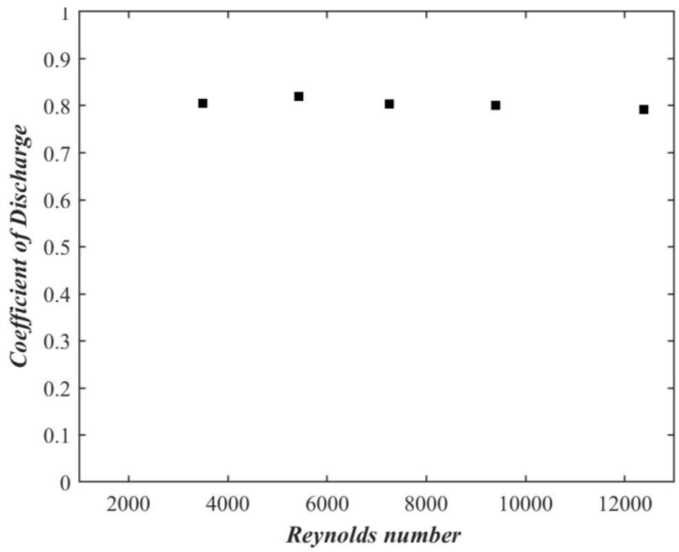

Figure 5.1: Coefficient of Discharge vs Reynolds number

5.2 Validation of experimental setup and numerical results

Jet impingement heat transfer experiments were repeated thrice for each test coupon for Reynolds numbers ranging from 3000 to 12000 with jet-to-jet spacing $X/D_{jet} = 3$ and a jet-to-target spacing of $Z/D_{jet} = 1$. The average of temperature registered by the four k-type thermocouples located beneath the top surface was considered as T_w in equation (1) for heat transfer calculations. The non-dimensional heat transfer coefficient of smooth target plate obtained from area averaged heat transfer coefficient was calculated by using equation (2). The results were then validated against the results presented in **Singh et al.** [34]. The experimental results were a super close match with a maximum error of 4.5% at $Re = 12000$ and an average error of 4% was observed. The non-dimensional heat transfer data computed from numerical models using equation (14) was then compared with experimental results.

Numerical analysis of smooth target plate was carried out with the same geometry and boundary conditions that of experimental test section as described in section 3&4. Area averaged heat transfer coefficient was calculated using the wall temperature of top plate as T_w in equation (1) and averaging the result over top surface. The non-dimensional heat transfer coefficient obtained from the average heat transfer coefficient matched well with the experimental results. Moreover, the correlation for Nusselt number Nu_b given by **Singh et al.** [34] was in accordance with the numerical and experimental values. The maximum error between numerical and experimental Nusselt number was found to be 7% at $Re = 12000$ and an average absolute error of 3% throughout the range of Reynolds numbers.

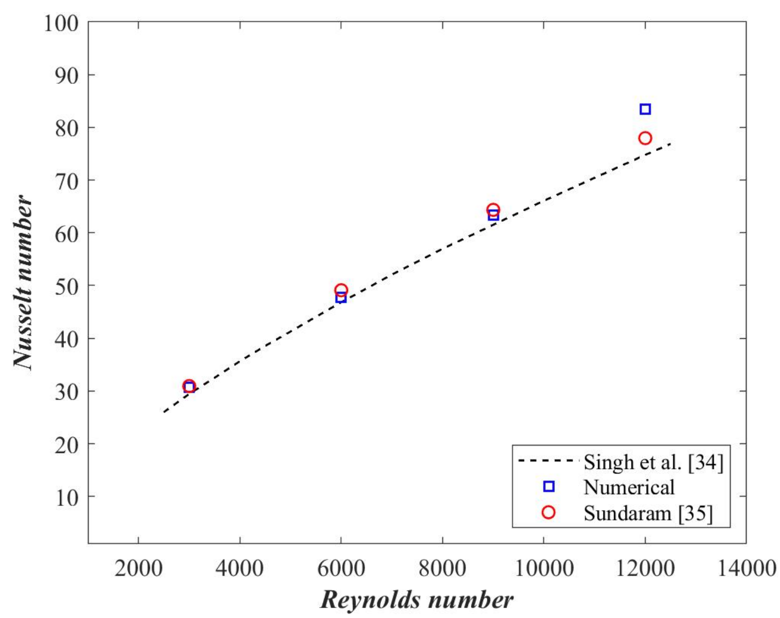

Figure 5.2: Validation of experimental and numerical non-dimensional heat transfer coefficient with **Singh et al.** [34] and **Sundaram**[35].

5.3 Jet impingement on a smooth target plate

Jet impingement heat transfer study on a smooth target plate is a widely researched topic in the field of electronics cooling. In this section heat transfer characteristics at wall are discussed with the help of contours of heat transfer coefficient. As shown in Figure **5.3**, the regions under the jets exhibit a high heat transfer coefficient visible in bright red and yellow. This is because the coolant air from jets directly impinges on these regions removing heat from the top surface. Hence, these regions have more access to the fresh coolant air and as a result are at a lower temperature compared to the rest of target plate. The regions of cross flow between the jets are known as recirculation zones and can be observed clearly as heat transfer coefficient is high across these regions.

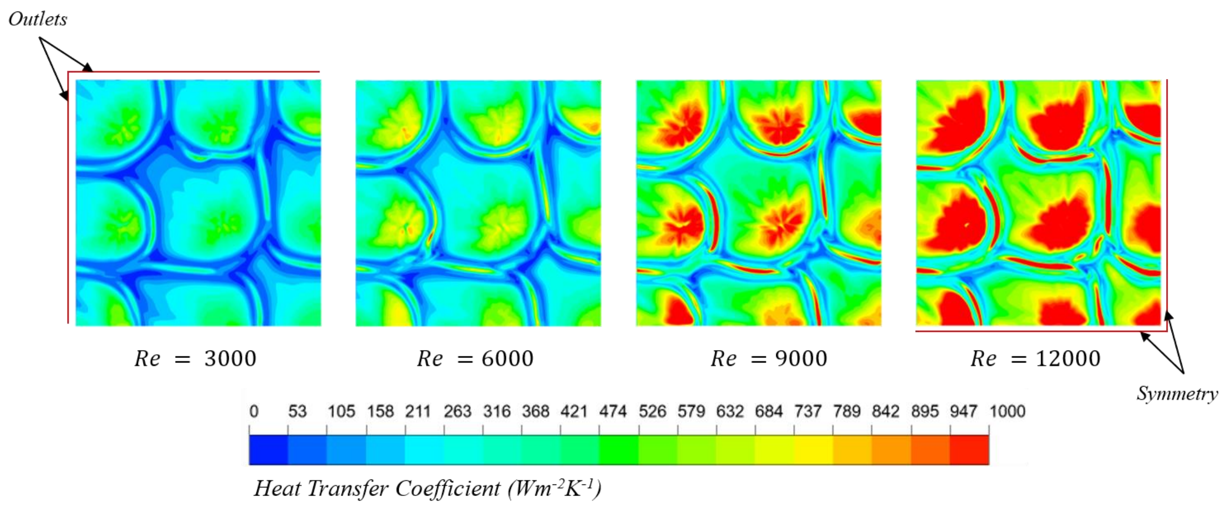

Figure 5.3: Heat transfer coefficient contours at the top surface of the smooth target plate at $Re = 3000$ (left most), $Re = 6000$ (second from left), $Re = 9000$ (third from left) and $Re = 12000$ (right most)

When observed closely, it is clear that the size of red and yellow spots beneath jets increase in the direction of cross flow. As expected, heat transfer coefficient is the highest in case of $Re = 12000$ and decreases from $Re = 12000$ to $Re = 3000$. The region of crossflow becomes more evident at $Re = 12000$ than $Re = 3000$. The HTC contours closely resemble a honeycomb like structure but with square sections. This is because of the arrangement of jets which are aligned in rows and columns akin to a uniformly spaced grid on a square. Furthermore, with in these recirculation zones, heat transfer coefficient keeps decreasing starting high at center and low at boundaries. This can be explained by the formation of vortices in the wall jet region which cause the flow to move away from top surface and into the cross flow region directly.

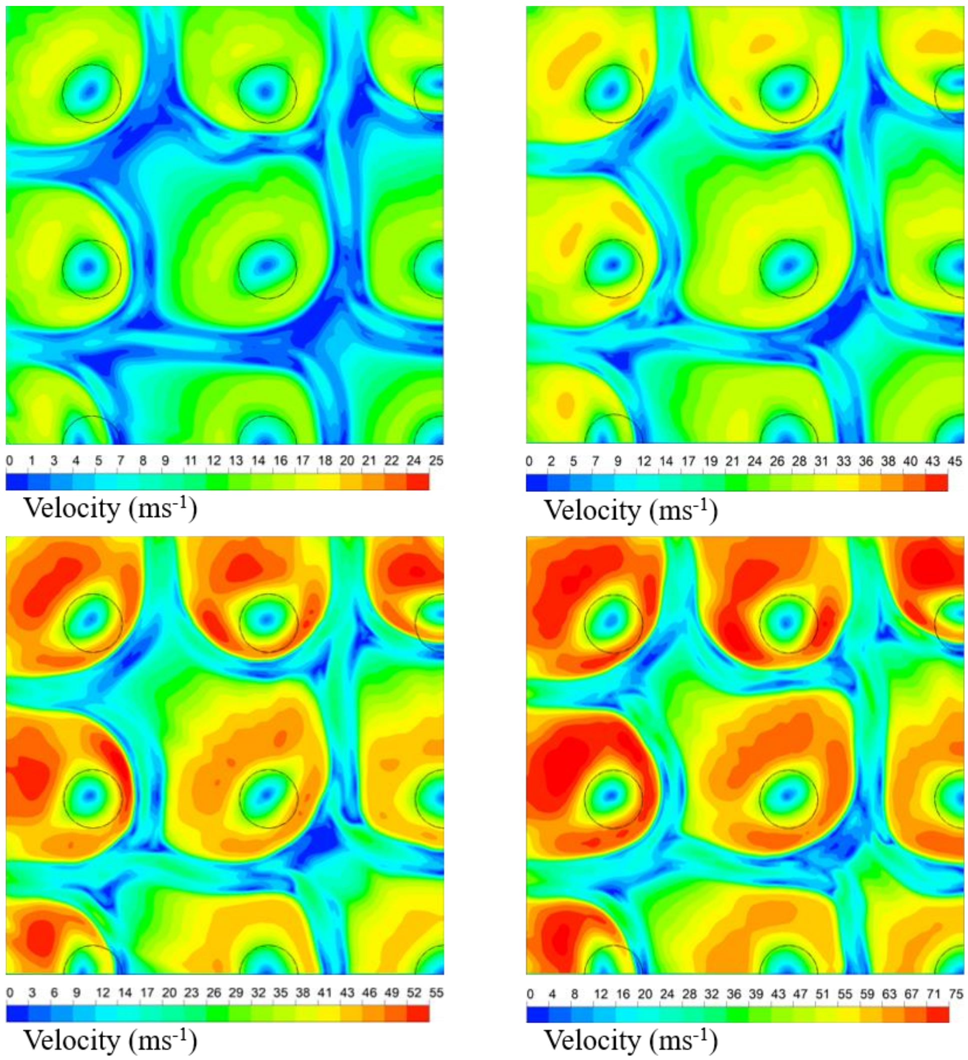

Figure 5.4: Contours of velocity 0.1 mm from top surface of the smooth target plate at $Re = 3000$ (top left), $Re = 6000$ (top right), $Re = 9000$ (bottom left) and $Re = 12000$ (bottom right)

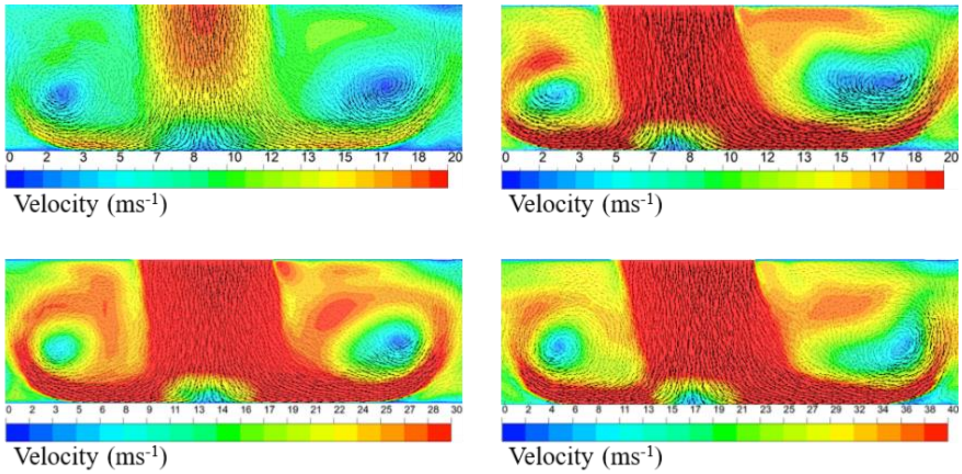

Figure 5.5: Contours of velocity superimposed on velocity vectors on a plane bisecting the top left jet onto a smooth target plate at $Re = 3000$ (top left), $Re = 6000$ (top right), $Re = 9000$ (bottom left) and $Re = 12000$ (bottom right)

The cross flow between jets and flow in jet wall region are also studied in addition to the effect of Reynolds number on heat transfer. For flow visualization, velocity contours are plotted at a distance of $0.1mm$ from the top surface of target plate shown in Figure **5.4**. The recirculation zones discussed above are much more visible in Figure **5.4**. The magnitude of velocity inside these sections increase in the direction of cross flow both in x and y directions. To study the flow in jet wall and stagnation region, velocity contours and vectors were plotted on a plane bisecting the first jet from top left corners shown in Figure **5.5**. The circles in velocity contours shown in Figure **5.5** are the circular jets and zones directly beneath jets. As the air from jet hits top surface of the target plate, it stagnates, and this is the reason the zones below jets are at low velocity than surroundings. This stagnation region is much more visible in Figure **5.5** in the shape of a small bubble like region under the bright red jet region. The vortices can be observed in wall jet region in figure above. These large eddies formed as a result of skin friction of target plate are crucial in dissipating heat.

5.4 Actual vs Intended numerical models of Cylindrical pin fins

Experiments with the test coupon containing cylindrical micro pin fins was carried out under same conditions as the smooth test coupon. However, the results from numerical analysis of intended geometry of the cylindrical pin fin test coupon did not match with experimental values. A significant deviation in area averaged HTC and non-dimensional HTC values was observed. The intended geometry overpredicted Nusselt number by an average of 32% with a maximum error of 36%. The values of Nusselt number calculated from experiments and numerical analysis are shown in Table **5.1** .Whereas the numerical analysis of actual geometry modelled using the data from profilometry produced a set of results that were way more accurate than earlier analysis. The maximum error in Nusselt number was only 8.4% with an average error of 5.3%. The deviation between intended and actual numerical models was enormous with a maximum deviation of 45% and an average deviation of 39%. Hence, the actual numerical model is deemed more reliable for studying the heat transfer characteristics. Figure **5.6** paints a better picture of the trends in Nusselt number at different Reynolds numbers.

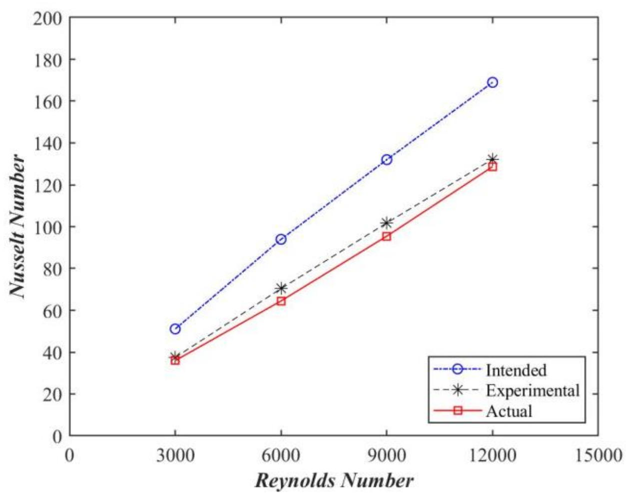

Figure 5.6: Nusselt number vs Reynolds number of the intended, actual numerical models and experimental results

Table 5.1: Variation of Nusselt number with Reynolds number calculated from intended and actual numerical models, deviation from the experimental Nusselt number

Reynolds number	3000.00	6000.00	9000.00	12000.00
Actual Nusselt number	35.96	64.47	95.45	128.67
Intended Nusselt number	51.08	93.93	132.01	168.97
Experimental Nusselt number	37.46	70.39	101.79	132.24
Error between Actual and Experimental	4.00%	8.41%	6.23%	2.70%
Error between Intended and Experimental	36.36%	33.44%	29.69%	27.78%
Deviation between Intended and Actual	42.05%	45.70%	38.30%	31.32%

5.4.1 Velolcity Contours of Intended and Actual Numerical Models

The velocity contours of actual numerical analysis reveal the true flow physics of jets near the surface of target plate. From the figure below it is clear that air is trapped in these square like blocks between the interconnections and pin fins. The velocity is in these blocks in almost 0 at $Re = 3000$, and increases with Reynolds number. The intended case predicts a vivid crossflow pattern that is likely to happen if there were no interconnections between micro pin fins and is very misleading because, in reality the flow is stagnant due to the interconnections between pin fins. This is the reason behind overprediction of intended numerical model.

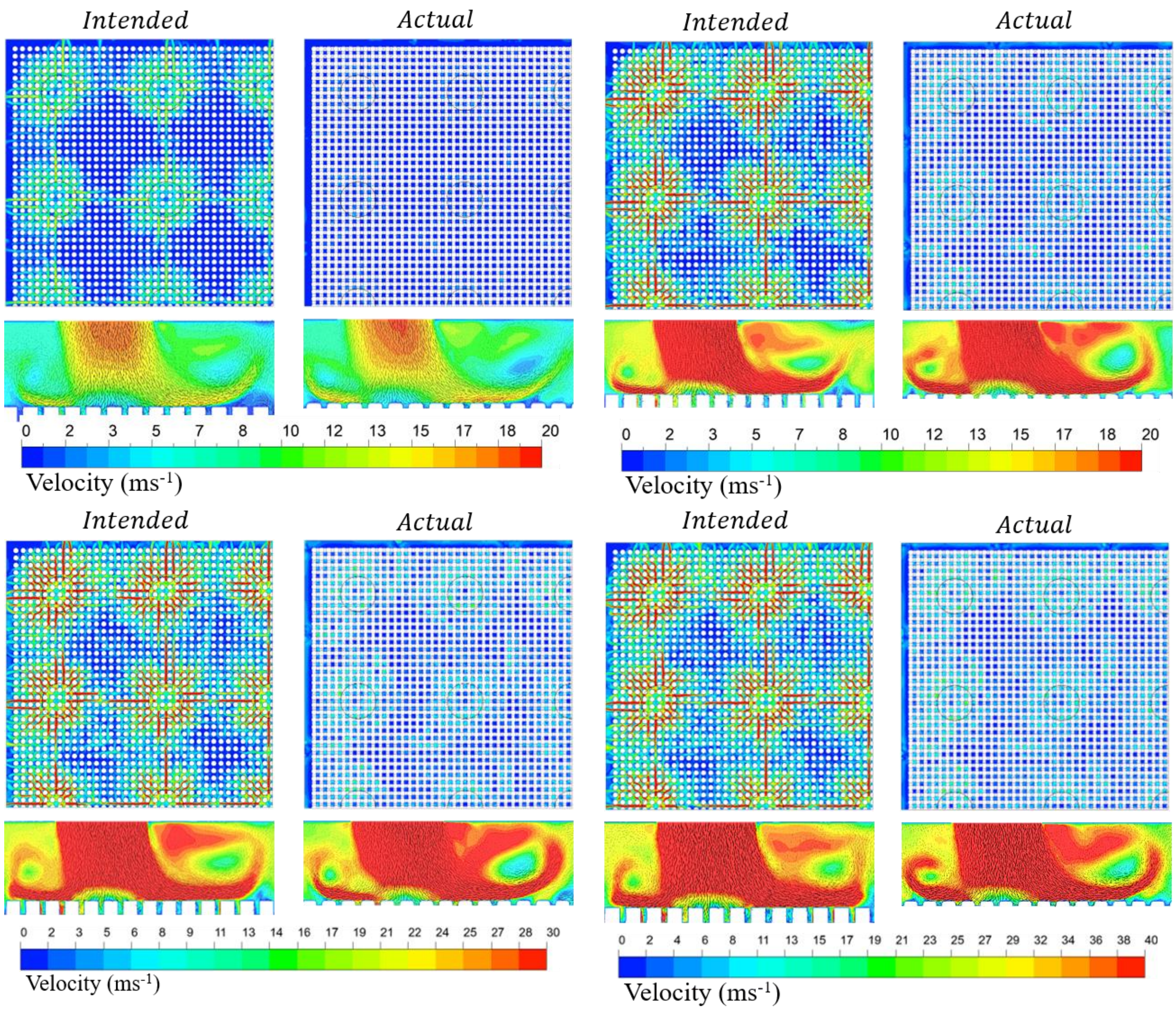

Figure 5.7: Comparison of velocity contours and vectors at 0.1 mm from top surface of intended and actual numerical models at $Re = 3000$ (top left), $Re = 6000$ (top right), $Re = 9000$ (bottom left) and $Re = 12000$ (bottom right)

Due to the interconnections, and the air trapped between them and pin fins cylindrical test coupon acted as if it was a smooth plate with micro pin fins of $1/5^{th}$ the actual height. This is clear from the velocity contours of jets where there is no flow across the space between pin fins. Rather the activity of vortices is higher than intended case because of less apparent jet-to-target spacing. The same reason is responsible for a bigger wall jet region and the rapid decay of jet.

5.4.2 Heat Transfer Characteristics

The contours of heat transfer coefficient of top surface of test coupon are attached in Figure **5.8**. The absence of crossflow near top surface of test coupon affected heat transfer coefficient by a huge margin. The intended geometry predicted a high HTC around the wall jet region due to high velocities. But actual case tells a different story as the air is essentially trapped between micro pin fins, the extra surface area of micro pin fins contributes very little to convective heat transfer. Only the top surface of micro pin fins are dissipating heat through convection and the rest of the wetted surface area is dissipating heat majorly through conduction rather than convection. As the flow between pin fins is almost nonexistent. The fraction of pin fins participating in heat dissipation increased with increasing Reynolds number as expected due to the increased amount of air supply. In actual case, pin fins in the cross flow region exhibit a higher heat transfer rate compared to intended case. A Spanwise study of heat transfer coefficient was done at $Re = 6000$ using the same 10 lines used for grid convergence study described in section 4. The average error in heat transfer coefficient was 20% with a maximum error of 43.5% at second line. This line is the closest to center of jet out of all the lines and as expected the difference in prediction is also the greatest.

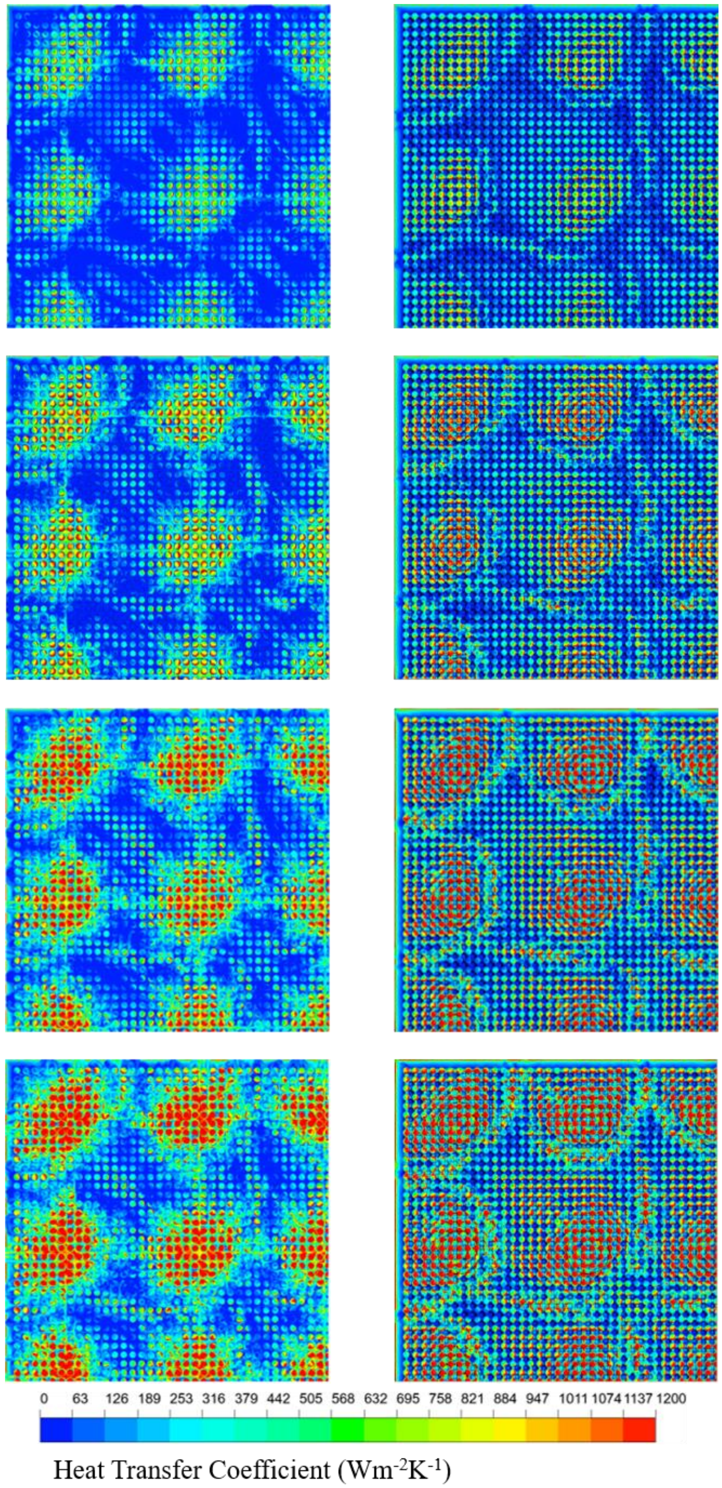

Figure 5.8: Comparison of contours of heat transfer coefficient at the top surface of intended and actual numerical models at $Re = 3000$ (top left), $Re = 6000$ (top right), $Re = 9000$ (bottom left) and $Re = 12000$ (bottom right)

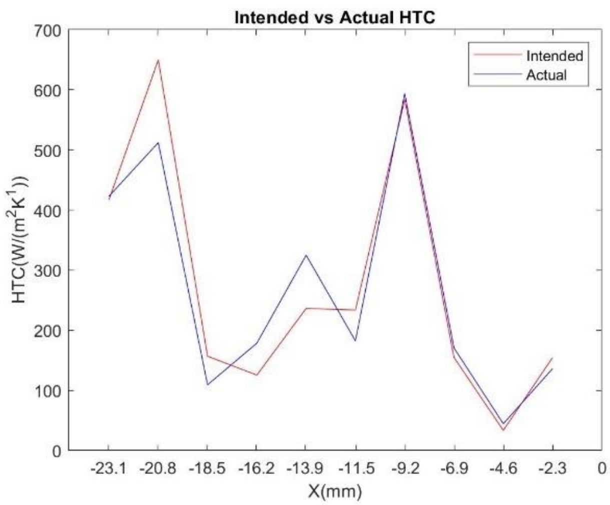

Figure 5.9: Line averaged heat transfer coefficients of intended and actual models along the spanwise direction of the top surface of target plate at $Re = 6000$

5.4.3 Conjugate vs Non-conjugate numerical models

All the numerical simulations performed so far were conjugate as the computational domain consisted of both fluid and solid domains. A non-conjugate numerical study without the target plate was also performed to check the viability of non-conjugate simulations. The non-conjugate simulation was carried out at $Re = 6000$. Generally, the heat flux input given at bottom of target plate is distributed uniformly across the volume of target plate. But since two sides of target plate are given adiabatic condition and the other two are given symmetry condition. The only available surface for heat to dissipate is top surface of target plate. The heat available at top surface is a fraction of the input and can be calculated by dividing the total heat flux input by area ratio of top surface. Area ratio is defined as the total wetted surface area of the top surface divided by the area of bottom surface or top surface without pin fins. This new calculated heat flux was used as input at bottom surface of fluid domain in the non-conjugate case. Equation (17) used for evaluating the heat transfer coefficient is attached below.

$$h(x,y) = \frac{q_{conv}}{A_{smooth}(T_w(x,y) - T_{abmient})} \tag{17}$$

The q_{conv} in equation (17) is same as the input heat flux as it is evenly distributed throughout the area. Another non-conjugate simulation employing a constant temperature boundary condition was also performed. Temperature used was the area averaged temperature of top surface of solid domain in the conjugate case. The HTC contours shown in Figure **5.10**. Since, the heat flux input is given uniformly over bottom surface of the fluid domain, HTC is more evenly distributed in the non-conjugate case compared to conjugate case. In the conjugate case heat flux emanating from top surface would be concentrated near jets. This is the major difference between the conjugate and non-conjugate cases as the difference in magnitude of the non-dimensional heat transfer is only 3%. But the contours of HTC look way different because of the uniform heat flux input in non-conjugate case. It was hypothesized that heat flux and temperature at the top surface will complement each other in such a way that heat transfer coefficient remain same as the conjugate analysis. However, it was observed that this holds true only for the area averaged heat transfer coefficient but not locally.

Non-conjugate analysis with constant temperature at the bottom surface was also carried out. The temperature of top surface of target plate was found to be constant in the conjugate analysis. This temperature of $343\ K$ was given as input for the second non-conjugate case. The deviation in area averaged HTC was found to be only 0.5% and HTC contours also look identical. The plot of line averaged HTC along spanwise direction is shown in Figure **5.11**. The average absolute deviation between the conjugate and non-conjugate constant flux cases was 22% with a maximum deviation of 50%. This goes to show that even though the global HTC values are in a good agreement, local HTC values and HTC contours can vary. The deviation of non-conjugate constant temperature case from conjugate was only 4%. Looking at the temperature contours in

Figure **5.10**, can provide more insights into understanding the ongoing physics. The wall temperature of the top surface of the target plate in conjugate simulations is almost at a constant temperature. Temperature of the layer of fluid in contact with top surface of solid domain remains at the same temperature as top surface. The top surface is coupled with the bottom surface of solid domain with a constant heat flux input at the bottom surface. But, due to the high thermal conductivity of aluminum, the solid domain acts as a lumped body and reaches constant temperature very early. Hence, in this case non-conjugate analysis with constant temperature describes the flow physics better than non-conjugate constant heat flux boundary condition case.

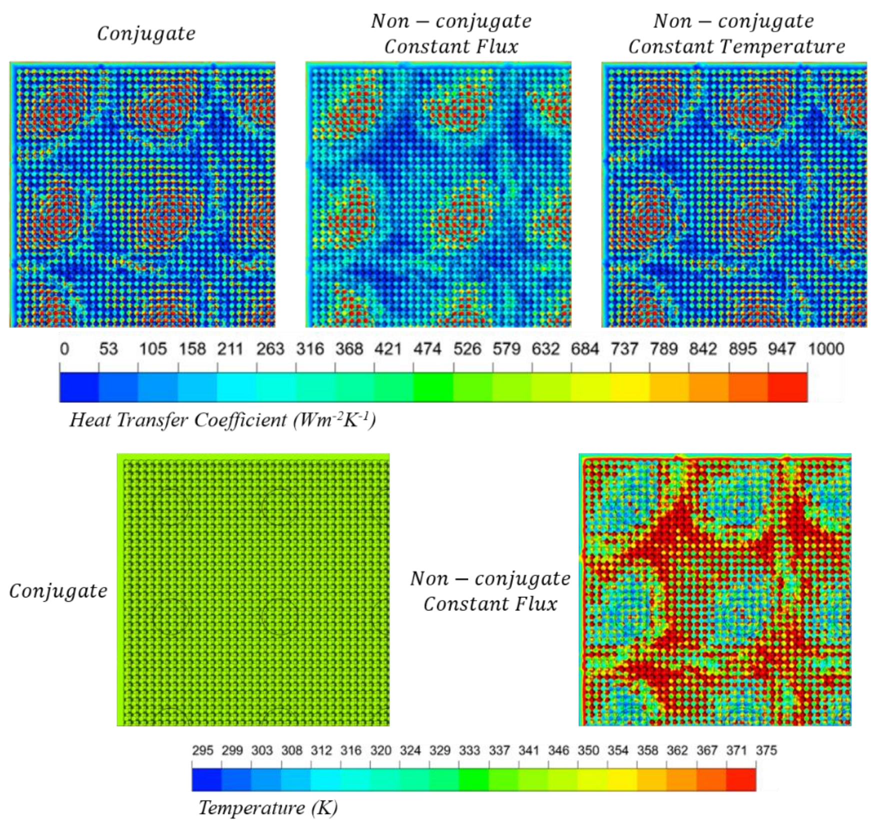

Figure 5.10: HTC contours (top) and Temperature contours (bottom) of conjugate (right), non-conjugate constant temperature (left) and non-conjugate constant flux (middle) numerical models at $Re = 6000$

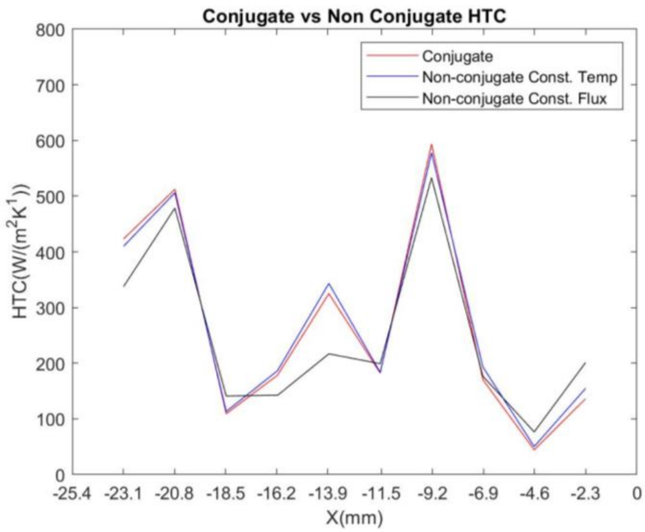

Figure 5.11: Line averaged HTC plot along spanwise direction of conjugate and non-conjugate constant flux and non-conjugate constant temperature numerical models at $Re = 6000$

5.5 Pyramidal pin fins Intended vs Actual Numerical Models

Cold spray is another additive manufacturing technique which uses a high-power jet to bombard the powder particles with a base plate and craft models. **Dupuis et al.** [20] conducted a forced convective heat transfer study on a target plate with pyramidal pin fins at $Re = 500$ through 2000. As discussed in section 3, they reported a high degree of deformation across the edges of pin fins and along slant height direction. In this study a numerical analysis was carried out using an intended geometry of the pyramidal pin fins as well as an approximation of what the final product of AM process might look like. The later model is referred as actual geometry in this study. For simplicity, only the deformation on edges is addressed. Due to the lack of experimental data, the numerical analysis was carried out only for $Re = 3000$ and 6000. Non-dimensional heat transfer coefficient was calculated by using equation (2) for both the cases. Figure **5.12** shows the plot of Nusselt numbers vs Reynolds number of intended and actual cases. The experimental data presented in **Dupuis et al.** [22] and an extrapolation of the best fit line with an $R^2 = 0.97$ is also plotted in Figure **5.12** .Error bars are plotted within 95% confidence level.

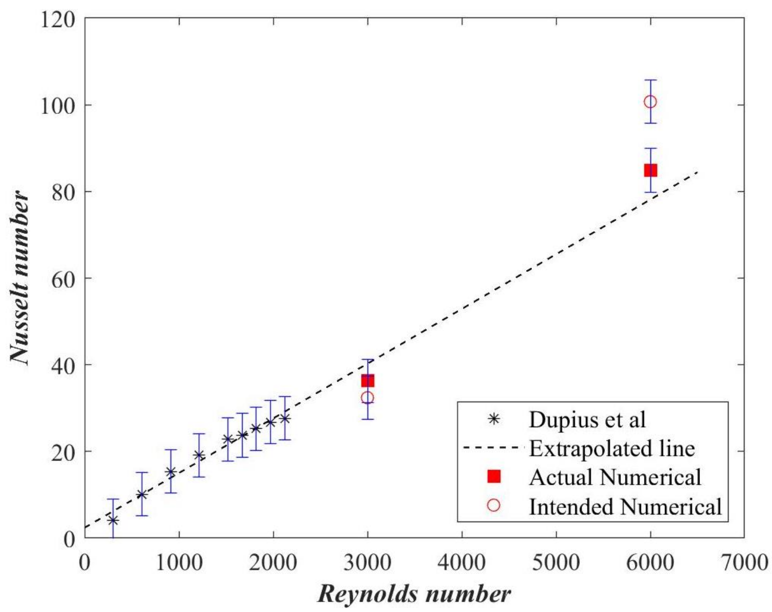

Figure 5.12: Comparison of intended and actual numerical models with experimental data presented in **Dupuis et al.** [22]

The Nusselt number from actual numerical models was closer to the predicted experimental value than intended numerical models with an error of about 10% at $Re = 3000$ and $Re = 6000$. The prediction from the numerical model of intended case had an error of 19.5% at $Re = 3000$ and 28.9% at $Re = 6000$. Nusselt number obtained from the intended numerical model deviated from the actual case by 9.6% at $Re = 3000$ and 18.6% at $Re = 6000$. This difference in the values of global non dimensional heat transfer coefficient can be accounted to the surface modifications. The heat transfer coefficient contours of both intended and actual cases are shown below in Figure **5.14**.The regions under jet exhibit a higher HTC as discussed earlier. But the actual case has a more uniform distribution compared to intended case. This becomes obvious while looking at blue regions.

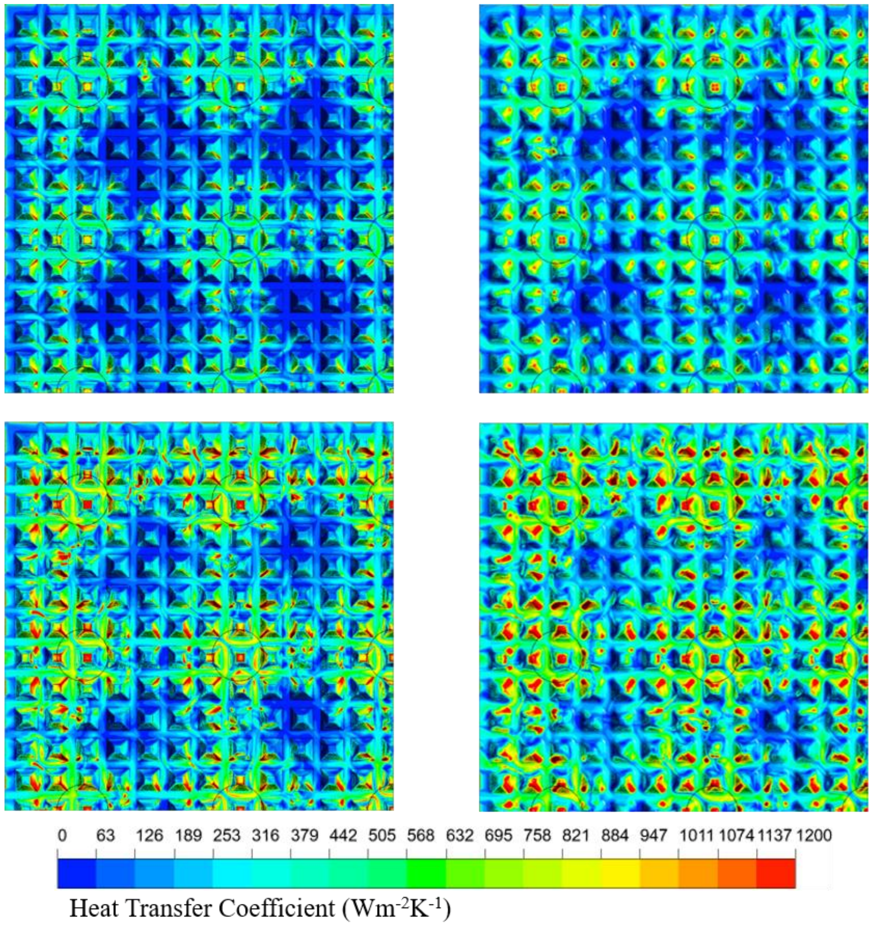

Figure 5.13: HTC contours of intended (left), actual (right) numerical models of pyramidal pin finned target plate at $Re = 3000$ (top) and at $Re = 6000$ (bottom).

The sharp edges present in intended case create a sharp pressure gradient across the edges whereas, the curved edges in actual case make it easier for the flow to get around. This is one of the major differences in the flow physics between the models and can be observed in the velocity contours in Figure **5.14** .The bright red regions in velocity contours shown in Figure **5.14** are more prominent and extend farther in actual case than intended case. At $Re = 3000$, actual numerical case predicted a higher area averaged HTC value than intended case. However, intended numerical case predicted a higher area averaged HTC value than actual case at $Re = 6000$. This disagreement can be resolved by observing two factors affecting global HTC value. Firstly, the area ratio and second the flow physics. At low Reynolds number, the flow physics seem to dominate and due to better flow, HTC is higher in actual numerical model. However, as the Reynolds number increases the effects of area ratio dominates, as area ratio of intended case is 1.60 and actual case has only an area ratio of 1.45. A 25% reduction in the wetted surface area compared to intended case caused the global HTC value to plummet.

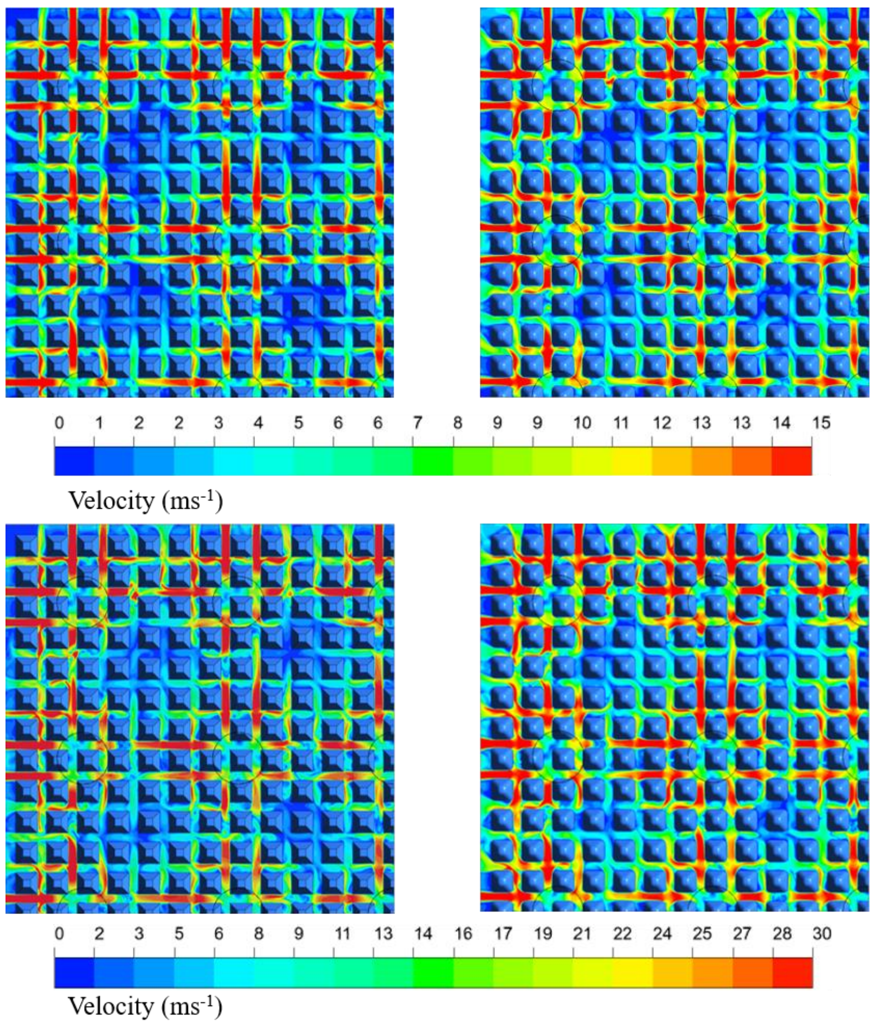

Figure 5.14: Velocity contours of the actual (left) and the intended (right) numerical models of pyramidal pin finned target plate at $Re = 3000$ (top) and $Re = 6000$ (bottom)

The velocity vectors overlapped on contours of velocity under jet present at the center of domain are shown in Figure **5.15**. The sharp edges cause poor wake regions and hence the flow into gaps between pin fins is obstructed. The same can be seen from the contours on left in Figure **5.15**. As the flow disperses from jet along two main perpendicular channels the flow into auxiliary channels is low in intended case than actual case. The velocity vectors overlapped on velocity contours beneath the first jet from top left corner are shown in Figure **5.16**. The stagnation region under the jet can be observed in both the models but in actual case more flow can be seen between pin fins than intended case. Again, sharp edges are responsible for the formation of bigger vortices in the flow due to steep pressure gradients.

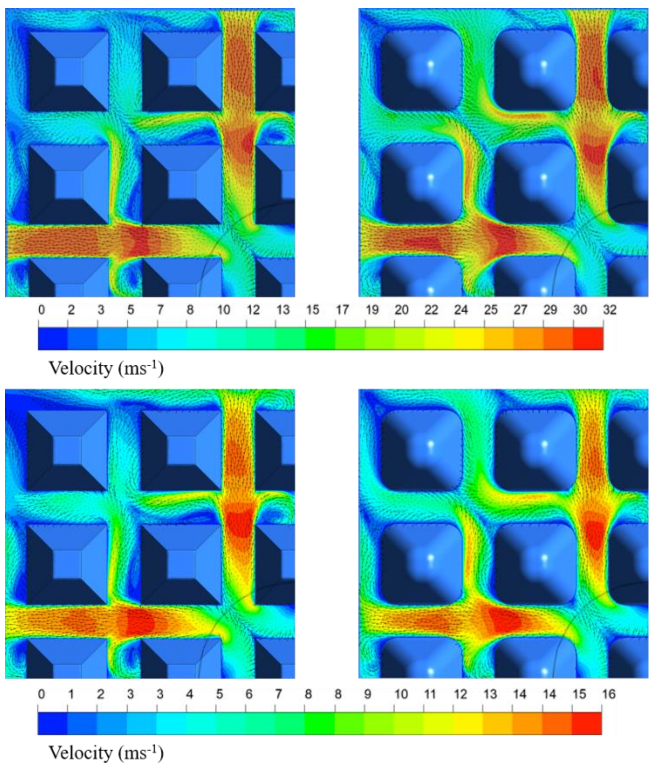

Figure 5.15: Velocity vectors superimposed on velocity contours of actual (right) and intended (left) beneath the jet at the center of the domain at $Re = 3000$ (top) and at $Re = 6000$ (bottom)

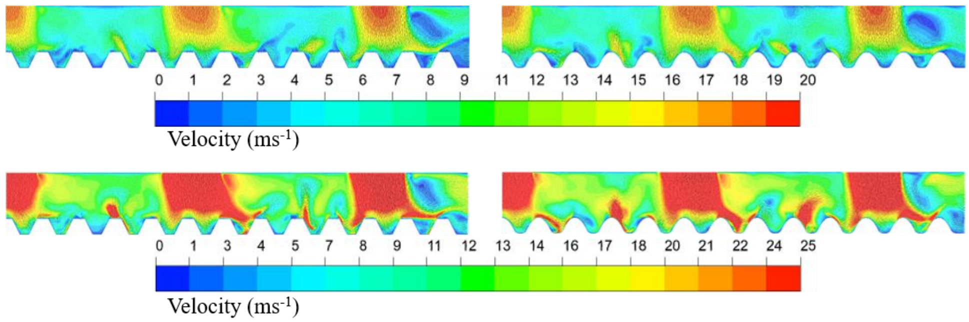

Figure 5.16: Velocity vectors superimposed on velocity contours of actual (right) and intended (left) on a plane bisecting the left most array of jets at $Re = 3000$ (top) and at $Re = 6000$ (bottom)

5.6 Pin fin effectiveness

Pin fin effectiveness was calculated using equation (15) described in section 4. Pin fin effectiveness was defined as the ratio of product of area averaged heat transfer coefficient and wetted area of rough test coupons to that of smooth test coupon. Studying the pin fin effectiveness is crucial as it helps in visualizing the increase in heat transfer rate due to the added extra surface area of pin fins. The pin fin effectiveness increases with increase in Reynolds number, but the slope flattens eventually. It is obvious from the plot shown in Figure **5.17** that intended cases of both cylindrical and pyramidal pin fins over predict the pin fin effectiveness by an average of 0.5. This goes into showing the importance of studying the profile of surface of AM parts. Pyramidal pin fins have a higher effectiveness than cylindrical pin fins at $Re = 6000$. However, the pin fin effectiveness is a global variable as it involves area averaged heat transfer coefficient. The non-conjugate case is almost overlapping with actual value for the same reason.

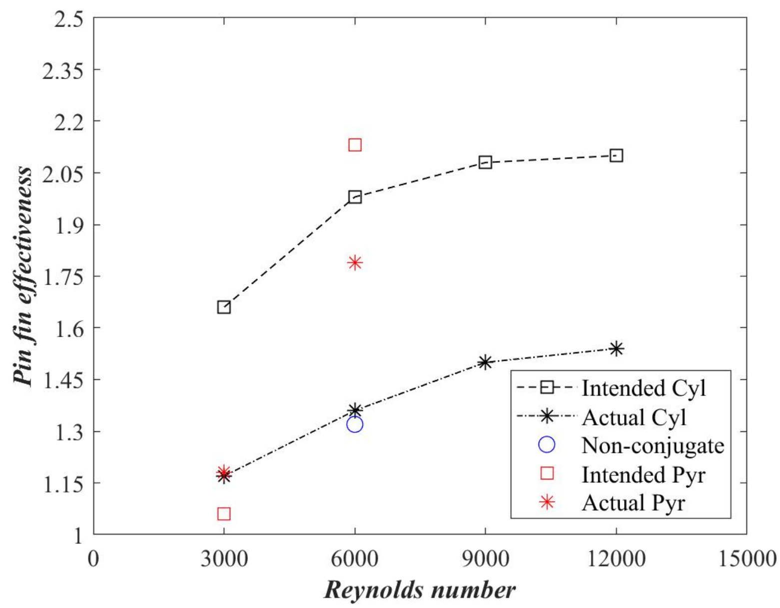

Figure 5.17: Pin fin effectiveness vs Reynolds number of all the numerical models

5.7 Pumping Power and Pressure Drop Characteristics:

The thermo-hydraulic performance of the target plates is calculated from the pin fin effectiveness and the pumping power required to maintain the flow at required mass flow rate corresponding to the given Reynolds number. Equation(18) was used to evaluate the pumping power. n_{jets} is the number of jets in domain and is equal to 25, Δp is the pressure drop across the test section. The variation of pumping power with Reynolds number and pin fin effectiveness is shown in two different plots in the Figure **5.18** .

$$P = \left(0.25\pi\nu Re_{D_{jet}} D_{jet} \Delta p\right) \times n_{jets} \tag{18}$$

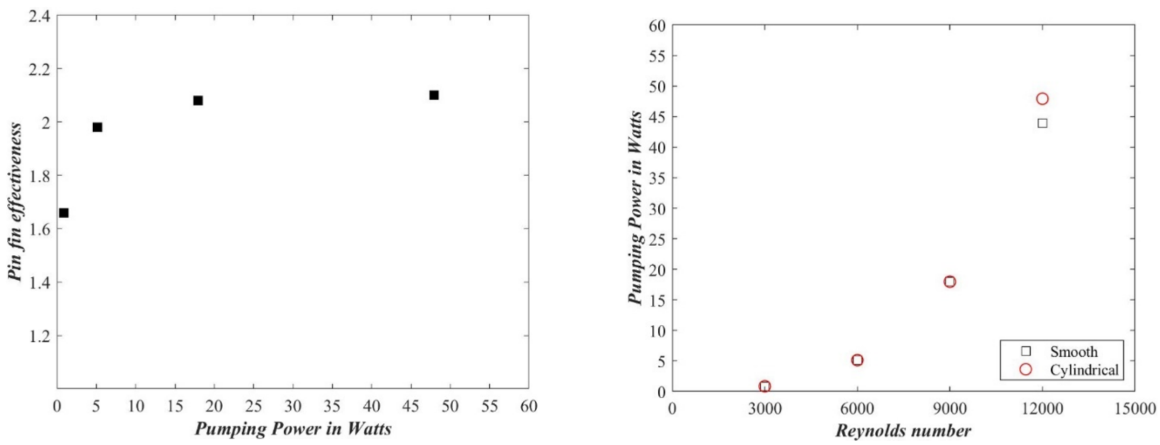

Figure 5.18: Pin fin effectiveness vs Pumping power in watts (left) of cylindrical pin finned target plate and Pumping power vs Reynolds number of smooth and cylindrical pin finned target plate (left)

The pumping power almost remains consistent for both the smooth and cylindrical test coupons as the difference can only be seen at $Re = 12000$. The plot of pin fin effectiveness vs pumping power is more insightful. After $Re = 9000$, the pumping power increases drastically but the pin fin effectiveness remains almost the same. While choosing a configuration of roughness for a given operating conditions, a comprise between the pumping power and pin fin effectiveness is crucial.

CONCLUSION AND RECOMMENDATIONS

Additive manufacturing is a budding technology, very little is known about the microstructures of the components produced using various AM techniques. Our understanding of several AM process is limited but quantifying major surface imperfections such as interconnections and troughs might prove to be useful.

- The contour of AM component is a stepped approximation of the intended CAD model. As a result of this, all parts manufactured by AM processes exhibit a staircase effect which cannot be fully eliminated and becomes prominent at smaller length scales.
- Surface imperfections that arise due to staircase effect and many other factors may impact the thermohydraulic performance of AM components. Numerical analysis of the intended geometry may not accurately predict the flow and heat transfer characteristics in such cases. Therefore, studying the surface topology of AM components is of great importance.
- In this thesis cylindrical micro roughness elements on a smooth target plate were printed using DMLS. The surface imperfections i.e., interconnections between pin fins were characterized and were integrated into the numerical analysis.
- The difference in flow physics and heat transfer characteristics was then studied from the standpoint of electronics cooling using jet impingement. A comprehensive study on surface roughness and the importance of various variables was discussed in section 3.
- The process of modelling better numerical models using profilometry was discussed in sections 3 and 4. The actual numerical model was 25% more accurate than the intended numerical model in predicting the value of area averaged Nusselt number.
- The test coupon with cylindrical pin fins performed best at $Re = 9000$ with a pin fin effectiveness of 2.1 but the pumping power required was 4 times greater than that was required

for $Re = 6000$ which exhibited a pin fin effectiveness of 2. Hence $Re = 6000$ was regarded as the better alternative out of all the test configurations.

- The numerical analysis of pyramidal pin finned case also conveyed a similar behavior of the intended case overpredicting the Nusselt number by 18% compared to the actual case. Non-conjugate analysis with a constant heat flux boundary condition of the actual geometry predicted Nusselt number to a good accuracy but failed in representing the local heat transfer characteristics.
- The area averaged and the local heat transfer characteristics predicted by the non-conjugate analysis using a constant temperature boundary condition matched closely with that of conjugate analysis.

Recommendations for future studies:

1. Test coupons with pyramidal pin fins and triangular wedges can be manufactured using DMLS and study the variations in the intended and actual geometries using a confocal laser microscope.
2. Investigate the microstructures of AM processed components and work on better 3D reconstruction to improve the accuracy and spectrum of numerical modelling of AM parts.
3. Different materials with low thermal conductivity can be explored for testing the viability of non-conjugate simulations over conjugate simulations.

NOMENCLATURE

A	area
C_d	coefficient of discharge
D	Diamter
D_h	hydraulic diameter
D_{jet}	diameter of the cylindrical jet nozzle
E	estimated fractional error
F_S	Factor of safety
GCI	Grid Convergence Index
h	heat transfer coefficient
$\bar{h}$	area averaged heat transfer coefficient
H	pin-fin height
l_r	length of the curve
$\dot{m}_j$	mass flow rate through jet
Nu	Nusselt number
Δp	pressure drop across test section
P	pressure
q_{conv}	convective heat transfer rate through wetted surface area

r	grid refinement ratio
R	universal gas constant
R_a	arithmetic mean height along a line
$Re_{D_{jet}}$	jet Reynolds number
R_q	root mean square height along a line
R_z	maximum height along a line
S	center-to-center pin-fin spacing
S_a	arithmetic mean height along a surface
S_q	root mean square height along a surface
S_z	maximum height along a surface
T_{aw}	mainstream temperature
T_w	target plate temperature
X/D_{jet}	normalized jet-to-jet spacing
Z/D_{jet}	normalized jet-to-target plate spacing
γ	adiabatic constant
ε	relative error
ε_f	pin fin effectiveness
k_f	thermal conductivity of air

REFERENCES

[1] Steinberg, Dave S. 1991. *Cooling techniques for electronic equipment*. New York: Wiley.

[2] Kordyban, Tony, "Hot Air Rises and Heat Sinks: Everything You Know about Cooling Electronics Is Wrong," ASME Press, 1998.

[3] Womac, D., Ramadhyani, S., Incropera, F., "Correlating equations for impingement cooling of small heat sources with single circular jets," Transactions of the ASME, Vol. 115, pp 106-115, 1993.

[4] Wohlers, T. Additive Manufacturing and 3D Printing State of the Industry: Wohlers Report; Wohlers Associates Inc.: Fort Collins, CO, USA, 2011.

[5] Kruth, J.P.; Levy, G.; Klocke, F.; Childs, T.H.C. Consolidation phenomena in laser and powder-bed based layered manufacturing. CIRP Ann. Manuf. Technol. 2007, 56, 730–759.

[6] Kruth, J.P.; Mercelis, P.; Van Vaerenbergh, J.; Froyen, L.; Rombouts, M. Binding mechanisms in selective laser sintering and selective laser melting. Rapid Prototyp. J. 2005, 11, 26–36.

[7] Manfredi, D., Calignano, F., Krishnan, M., Cannoli, R., Ambrosio, E.P., Atzeni, E. "From Powders to Dense Metal Parts: Characterization of a Commercial AlSiMg Alloy Processed through Direct Metal Laser Sintering," *Materials* 2013, *6*, 856-869.

[8] Wright, C.S.; Dalgarno, K.W.; Dewidarin, M.M. Processing conditions and mechanical properties of high speed steel parts fabricated using direct selective laser sintering. Proc. Inst. Mech. Eng. B J. Eng. Manuf. 2009, 217, 1651–1663.

[9] Frazier, W.E. "Metal Additive Manufacturing: A Review," Journal of Materials Engineering and Performance, Vol. 23, No, 6, 2014, pp. 1917-1928.

[10] Simchi A., Petzoldt F., Pohl H., "On the development of direct metal laser sintering for rapid tooling," Journal of Materials Processing Technology, Vol. 141, No. 3, 2003, pp. 319-328.

[11] Simchi A., Pohl H., "Effects of laser sintering processing parameters on the microstructure and densification of iron powder," Materials Science and Engineering: A, Vol. 359, No. 1–2, 2003, pp. 119-128.

[12] Reimund Neugebauer, Bernhard Müller, Mathias Gebauer, and Thomas Töppel, "Additive manufacturing boosts efficiency of heat transfer components," Assembly Automation, Vol. 31, No. 4, 2011, pp. 344 – 347.

[13] Stimpson, Curtis K., Jacob C. Snyder, Karen A. Thole, Dominic Mongillo, "Roughness Effects on Flow and Heat Transfer for Additively Manufactured Channels," Journal of Turbomachinery, Vol. 138, No. 5, 2016, pp. 051008/1-10.

[14] Raghavan A., Wei H. L., Palmer T. A., and Debroy T., "Heat Transfer and Fluid Flow in Additive Manufacturing." Journal of Laser Applications, Vol. 25, No. 5, 2013, pp. 052006/1-8.

[15] B. Kwon, T. Foulkes, T. Yang, N. Miljkovic and W. P. King, "Air Jet Impingement Cooling of Electronic Devices Using Additively Manufactured Nozzles," *IEEE Transactions on Components, Packaging and Manufacturing Technology*, Vol. 10, No. 2, 2020, pp. 220-229.

[16] Luigi Ventola, Francesco Robotti, Masoud Dialameh, Flaviana Calignano, Diego Manfredi, Eliodoro Chiavazzo, Pietro Asinari, "Rough surfaces with enhanced heat transfer for electronics cooling by direct metal laser sintering," International Journal of Heat and Mass Transfer, Vol. 75, 2014, pp. 58-74.

[17] Snyder, Jacob C., and Karen A. Thole. “Tailoring Surface Roughness Using Additive Manufacturing to Improve Internal Cooling.” Journal of Turbomachinery, Vol. 142, No. 7, 2020, pp. 071004/1-12.

[18] Kirsch, Kathryn L., and Karen A. Thole. “Heat Transfer and Pressure Loss Measurements in Additively Manufactured Wavy Microchannels,” Journal of Turbomachinery, Vol. 139, No. 1, 2016, pp. 011007/1-9.

[19] Kirsch, Kathryn L., and Karen A. Thole. “Isolating the Effects of Surface Roughness versus Wall Shape in Numerically Optimized, Additively Manufactured Micro Cooling Channels,” Experimental Thermal and Fluid Science, Vol. 98, 2018, pp. 227–238.

[20] Philippe Dupuis, Yannick Cormier, Marianne Fenech, Bertrand Jodoin, “Heat Transfer and Flow Structure Characterization for Pin Fins Produced by Cold Spray Additive Manufacturing.” International Journal of Heat and Mass Transfer, Vol. 98, 2016, pp. 650–661.

[21] Philippe Dupuis, Yannick Cormier, Aslan Farjam, Bertrand Jodoin, Antoine Corbeil, “Performance evaluation of near-net pyramidal shaped fin arrays manufactured by cold spray,” International Journal of Heat and Mass Transfer, Vol. 69, 2014, pp. 34-43.

[22] Philippe Dupuis, Yannick Cormier, Marianne Fenech, Antoine Corbeil, Bertrand Jodoin, “Flow structure identification and analysis in fin arrays produced by cold spray additive manufacturing,” International Journal of Heat and Mass Transfer, Vol. 93, 2016, pp. 301-313.

[23] Yannick Cormier, Philippe Dupuis, Aslan Farjam, Antoine Corbeil, Bertrand Jodoin, "Additive manufacturing of pyramidal pin fins: Height and fin density effects under forced convection," International Journal of Heat and Mass Transfer, Vol. 75, 2014, pp. 235-244.

[24] Ferster, K. K., Kirsch, K. L., and Thole, K. A, "Effects of Geometry, Spacing, and Number of Pin Fins in Additively Manufactured Microchannel Pin Fin Arrays," Journal of Turbomachinery, Vol. 140, No. 1, 2018, pp. 011007/1-10.

[25] R.J. Goldstein, A.I. Behbahani, "Impingement of a circular jet with and without cross flow," International Journal of Heat and Mass Transfer, Vol. 25, No. 9, 1982, pp. 1377-1382.

[26] Holger Martin, "Heat and Mass Transfer between Impinging Gas Jets and Solid Surfaces," Advances in Heat Transfer, Volume 13, 1977, pp. 1-60.

[27] Zuckerman, N., and Lior, N., "Radial Slot Jet Impingement Flow and Heat Transfer on a Cylindrical Target," International journal of heat and fluid flow, Vol. 21, No. 3, 2007, pp. 548-560

[28] Zuckerman, N., and Lior, N., "Jet Impingement Heat Transfer: Physics, Correlations, and Numerical Modeling," Advances in Heat Transfer, Vol. 39, 2006, pp.565-631.

[29] Kercher, D.M. and Tabakoff, W., "Heat transfer by a square array of round air jets impinging perpendicular to a flat surface including the effect of spent air." Journal of Engineering for Power, Vol. 92, No. 1, 1970, pp. 73-82.

[30] Garimella, S.V. and Schroeder, V.P., 2000. Local heat transfer distributions in confined multiple air jet impingement. J. Electron. Packag., 123(3), pp.165-172.

[31] Jung yang San, Mao De Lai, "Optimum jet-to-jet spacing of heat transfer for staggered arrays of impinging air jets," International Journal of Heat and Mass Transfer, Vol. 44, 2001, pp. 3997-4007.

[32] Shan Yong, Zhang Jing-zhou, Xie Gong-nan, "Convective heat transfer for multiple rows of impinging air jets with small jet-to-jet spacing in a semi-confined channel," International Journal of Heat and Mass Transfer, Vol. 86, 2015, pp. 832-842.

[33] Madhavan, S., Ramakrishnan, K.R., Singh, P., and Ekkad, S., "Jet Impingement Heat Transfer Enhancement by U-Shaped Crossflow Diverters," Journal of Thermal Science and Engineering Applications, Vol. 12, No. (enter number here) , 2019 pp. 1-9.

[34] Singh P., Zhang M., Shoaib Ahmed, Kishore R. Ramakrishnan, Srinath Ekkad, "Effect of micro-roughness shapes on jet impingement heat transfer and fin-effectiveness," International Journal of Heat and Mass Transfer, Vol. 132, 2019, pp. 80-95.

[35] Sundaram R.D., "Enhanced fin-effectiveness of micro-scale concentric-shape roughened target surface subjected to array jet impingement," International Journal of Heat and Mass Transfer, Vol. 173, 2021, 121148.